A STUDY OF BACKGROUND RADIATION DISTRIBUTIONS FOR THE SLAC B FACTORY DRIFT CHAMBER

By

C.R. Cherie Goodenough

B.Sc. (Hon), University of Victoria, 1994

A THESIS SUBMITTED IN PARTIAL FULFILLMENT OF

THE REQUIREMENTS FOR THE DEGREE OF

MASTER OF SCIENCE

IN

THE FACULTY OF GRADUATE STUDIES

DEPARTMENT OF PHYSICS

WE ACCEPT THIS THESIS AS CONFORMING

TO THE REQUIRED STANDARD

....

....

....

THE UNIVERSITY OF BRITISH COLUMBIA

AUGUST 1996

Department of Physics
The University of British Columbia
6224 Agricultural Road
Vancouver, Canada
V6T 1W5

Date:

Abstract

The distribution of lost-particle and bremsstrahlung background radiation in the *BaBar* Drift Chamber at the Stanford Linear Accelerator Center (SLAC) has been modeled. Simulations show that occupancies are well within manageable levels (peaked at 0.55% in the inner layers) at nominal rates and that radical changes in the endplate design are unnecessary. Chamber aging is also shown to occur at an acceptable level, with no significant damage to the chamber wires within the first five years.

Table of Contents

List of Figures

Acknowledgments

Working at SLAC on the *BaBar* drift chamber project has been an exciting, educational and rewarding experience. This would not have been the case, however, were it not for the many wonderful people who have given me their support and friendship over the past four years, first as an undergraduate and later as a UBC student. I am glad to have this chance to thank some of the people who have been the most influential to me.

It is undoubtedly true that without Dale Pitman as a mentor and friend I would not only never have had the opportunity to work at SLAC, but I would also not have pursued my graduate degree in particle physics. I have been very lucky to have her as a teacher, advocate and role model. Thank you for everything, Dale.

My good fortune continued with having Janis McKenna as my supervisor. Janis has been an incredibly supportive, understanding and patient person to work for and I can't imagine having completed my degree without her help. Thanks, Janis, I should be so lucky as to have another boss like you.

There are many people at SLAC who have provided a great deal of help and encouragement. They are too many to name them all, so perhaps I will simply thank all of Group C. Requiring specific thanks, though are Art Snyder, Dave Coupal and Tom Mattison.

I would also like to express my thanks to the second reader on my thesis, Garth Jones. I appreciate the time and effort he has expended both as a teacher and a reader.

The wonderful friends that I have made during my days at SLAC have been a source of support and even, occasionally, actual information. The SLAC Spinors softball team includes almost everyone in this category. If it weren't for the Bridge Club (Jim 'Q'

Quigley, Dave Reyna, Greg Mitchell and Suzanne Komili) I might have finished this thesis months ago, but I would have had a lot less fun. And last, but not least, two people with whom it has been my honour to be acquainted with over the last few years, Jaret Heise and Mark McDougald, thanks for everything.

Foreword

A new storage ring (PEP-II) and detector (*BaBar*) are currently under construction at the Stanford Linear Accelerator Center. The physics goal for this new machine and detector is to measure the parameters of CP violation using the B meson system. Many small studies are required to optimize the design and performance of both the machine and the detector. A number of Canadian institutions, including the University of British Columbia, are contributing to the design and construction of the central tracking drift chamber component of the *BaBar* detector. This thesis is a detailed discussion of one of the studies carried out for the drift chamber group, namely modeling the distribution of background radiation in the drift chamber. The results of these studies were published in the *BaBar* Letter of Intent [11] and the *BaBar* Technical Design Report [12].

Chapter 1

Introduction

Why does the universe look the way it does? This complex question remains thus far unanswered. How did galaxies form? Is the universe going to expand forever from the Big Bang or will it all end with a Big Crunch? Why are there three generations of *quarks* and *leptons* with very different masses? Why is the universe made almost entirely of matter, not equal parts matter and antimatter? It is this last question that the *BaBar* collaboration at Stanford Linear Accelerator Center (SLAC) hopes to answer, at least in part. To that end, SLAC and a large group of other institutions (including the University of British Columbia) are currently designing and constructing an asymmetric, high-luminosity B-meson facility at SLAC.

The central topic of this thesis is a detailed study of the distribution of background radiation in a long central tracking chamber now under construction for *BaBar*. Specific design considerations will be addressed from the point of view of backgrounds. This study was undertaken using two Monte Carlo programs in work done at SLAC from 1993 to 1995.

Since the PEP-II e^+/e^- collider used by *BaBar* has several unique aspects to its design that seriously affect background radiation, there is a chapter discussing the machine design. These accelerator innovations are likewise motivated by the B physics to be studied at *BaBar*. Consequently, this introductory section will discuss the physics of CP violation and its study using the B system. There will also be a brief section defining the types of background radiation studied.

1.1 The Standard Model and the CKM Mixing Matrix

The Standard Model of particle physics is a very successful model for describing particles and their interactions via three of the four fundamental forces. These forces are the strong, the electromagnetic, and the weak. The theory of quantum chromodynamics (QCD) describes strong interactions and the electroweak theory describes a unification of the electromagnetic and weak interactions. For a more complete discussion of the Standard Model see [1, 2].

There are two types of particles described by the Standard Model, *fermions* (which make up matter) and *gauge bosons* (which mediate forces). Fermions are likewise separated into two distinct groups, *quarks* and *leptons*. Both quarks and leptons are spin 1/2, pointlike particles. One way in which quarks differ from leptons is that they carry *colour charge*, allowing them to interact via the strong interaction. A consequence of this colour charge is that quarks are never seen in unbound states, but only in three-quark bound states (*baryons*) and quark/antiquark bound states (*mesons*). This is a result of the fact that only colourless objects are seen in nature.

There are six *flavours* of quarks in the Standard Model, which are grouped into three *generations*:

$$\begin{pmatrix} u \\ d \end{pmatrix}, \begin{pmatrix} c \\ s \end{pmatrix}, \begin{pmatrix} t \\ b \end{pmatrix}.$$

The upper quark in each generation has charge +2/3e and the lower -1/3e. There are also six leptons, grouped into three generations. Each generation contains a massive particle with charge -1e and a corresponding massless, chargeless neutrino (denoted by ν):

$$\begin{pmatrix} e \\ \nu_e \end{pmatrix}, \begin{pmatrix} \mu \\ \nu_\mu \end{pmatrix}, \begin{pmatrix} \tau \\ \nu_\tau \end{pmatrix}.$$

Each quark and lepton has a corresponding antiparticle, denoted by a bar (ie. the antiparticle of a c quark is $\bar{c}$).

Fermions can interact via the weak force. This force is mediated by the Z^0 and $W^{\pm}$ gauge bosons. Weak interactions involving a Z^0 exchange are called *neutral currents* and those involving $W^{\pm}$ are called *charged currents*. The charged weak interaction is said to be *flavour changing* as a result of the fact that when a quark emits or absorbs a $W^{\pm}$ boson, the particle flavour changes to another quark flavour. In the case of leptons, the massive particle changes to the neutrino in its generation (or vise versa). For example, a u quark emits a W^+ and changes flavour to a d. This process is shown diagrammatically in Figure 1.1, an example of a *Feynman diagram*. Feynman diagrams are not only useful for depicting particle interactions, but are also powerful theoretical tools for the calculation of the probability that an interaction will occur. Throughout this thesis, the time axis in Feynman diagrams will point to the right.

Not only is the charged weak interaction flavour changing, it also allows "cross-generational mixing" of quarks, according to the Standard Model. This means that while a c quark can *decay* (ie. interact by emitting or absorbing a gauge boson) into an s quark, it might also decay into a d quark. This phenomenon is accommodated in the Standard Model by saying that the s quark is not an *eigenstate* of the weak interaction. The particle participating in the weak interaction (the weak eigenstate) is not the s quark, but rather a linear combination of the d, s, and b quarks (which are referred to as *mass* or *flavour eigenstates*). The charged weak interactions are incorporated into the Standard Model through the Cabibbo-Kobayashi-Maskawa (CKM) matrix. The weak

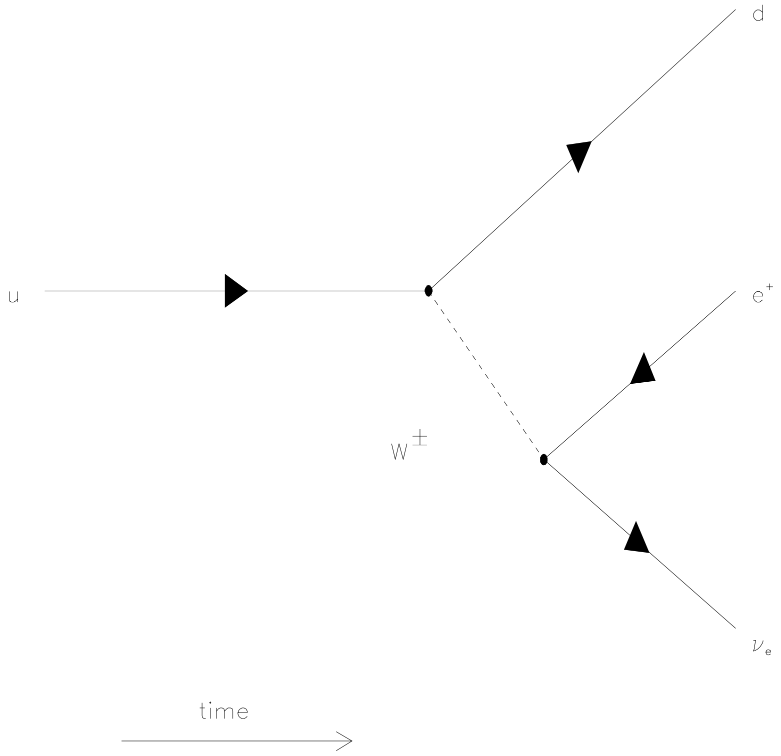

Figure 1.1: The u quark emits a W^+ changing its flavour to d. The W^+ then decays into a positron and an electron neutrino.

eigenstates, denoted by a primed symbol, are given by:

$$\begin{pmatrix} d' \\ s' \\ b' \end{pmatrix} = \begin{pmatrix} V_{ud} & V_{us} & V_{ub} \\ V_{cd} & V_{cs} & V_{cb} \\ V_{td} & V_{ts} & V_{tb} \end{pmatrix} \begin{pmatrix} d \\ s \\ b \end{pmatrix} \tag{1.1}$$

where

$$V = \begin{pmatrix} c_{12}c_{13} & s_{12}c_{13} & s_{13}e^{-i\delta_{13}} \\ -s_{12}c_{23} - c_{12}s_{23}s_{13}e^{i\delta_{13}} & c_{12}c_{23} - s_{12}s_{23}s_{13}e^{i\delta_{13}} & s_{23}c_{13} \\ s_{12}s_{23} - c_{12}c_{23}s_{13}e^{i\delta_{13}} & -c_{12}s_{23} - s_{12}c_{23}s_{13}e^{i\delta_{13}} & c_{23}c_{13} \end{pmatrix} \tag{1.2}$$

Here, $c_{ij} = \cos\theta_{ij}$ and $s_{ij} = \sin\theta_{ij}$ with i and j being "generation" labels 1, 2 and 3. CP violation enters in non-zero values of the phase δ_{13} [3] (more on this in Section 1.3.2). The convention of assigning the +2/3 mass eigenstates u, c, and t to also be weak eigenstates and the -1/3 weak eigenstates to be linear combinations of the -1/3 mass eigenstates is arbitrary. It should also be noted that the parameterization of V given by Equation 1.2 is valid only if there are exactly three quark families (as in the Standard Model). A 3×3 unitary matrix contains 3 free rotation angles (θ_{ij}) and one physical phase (δ_{13})[3].

The magnitudes of the elements of the CKM matrix have been determined experimentally. These are shown below, with 90% confidence limits [3]:

$$|V| = \begin{pmatrix} 0.9747 - 0.9759 & 0.218 - 0.224 & 0.002 - 0.005 \\ 0.218 - 0.224 & 0.9738 - 0.9752 & 0.032 - 0.048 \\ 0.004 - 0.015 & 0.030 - 0.048 & 0.9988 - 0.9995 \end{pmatrix} \tag{1.3}$$

Note that the diagonal elements are all approximately unity and that the elements V_{ub} and V_{td} are the smallest in the matrix. This implies that while the charged current weak interaction allows cross-generational mixing, this mixing is suppressed compared to flavour changing within a generation. In other words, the flavour changing charged current interaction $c \to d$ is suppressed relative to the $c \to s$ interaction. The $c \to d$

interaction is said to be *Cabibbo suppressed.* By the same argument, the interaction $b \to u$ is highly Cabibbo suppressed, owing to the very small magnitude of the V_{ub} element of the quark mixing matrix.

Finally, it is observed in charged current weak interactions that the $W^{\pm}$ couples only to *lefthanded* fermions and *righthanded* antifermions. A particle is said to be righthanded if its spin vector is aligned with its momentum vector, lefthanded if antialigned.

Charged current weak interactions, the CKM matrix and how CP violation is incorporated into the Standard Model will be discussed further in Sections 1.3 and 1.3.2.

1.2 The Matter/Antimatter Puzzle

As mentioned in Section 1.1, every particle has an antiparticle (although some neutral particles, like the photon, are their own antiparticles). In fact, particles and antiparticles are routinely created in collisions using particle accelerators. It is very interesting to note that matter and antimatter seem to be created in equal quantities by these high-energy collisions.

This observation is in direct contradiction to the evidence of the everyday world. Antimatter is rarely encountered outside of the particle accelerator. In fact, evidence suggests that the entire universe is composed of matter, with very little antimatter. Why is this? Did such an asymmetry exist from the moment of the Big Bang, or did this imbalance develop sometime later? If the latter, what is the mechanism for this imbalance to exist? But first, what is the evidence for the dominance of matter in the universe?

It is easily shown that matter and antimatter cannot exist in close proximity. A star made of half matter, half antimatter would annihilate immediately, all of its matter converted to energy. However, the possibility still exists that matter and antimatter might coexist if confined to isolated regions in the universe.

Simply looking at objects in the universe does not provide any answers about their composition. Since photons are their own antiparticles, photons created in interactions in a matter galaxy look identical to photons created in antimatter galaxies.

The same is not true for neutrinos, which have distinct antiparticles. While these certainly would mark whether the originating galaxy was composed of matter or antimatter, neutrinos are very difficult to detect since they are massless, chargeless and interact very weakly with matter.

Cosmic rays provide the first clue. These are high-energy particles that arrive at earth from space, mostly from objects within the Milky Way. Cosmic rays are composed almost entirely of particles, not antiparticles, indicating the the Milky Way is composed predominantly of matter. This argument also holds for the local group, a cluster of galaxies of which the Milky Way is a member.

For more distant galaxies, the evidence consists more of what is not observed. If a matter and antimatter galaxy were to collide, this would appear as a very strong source of gamma-ray emissions. Such sources are not observed, although several sources of gamma radiation are under investigation.

The most compelling argument, however, is that it is very difficult to imagine how matter and antimatter could have been created in equal quantities in the Big Bang and become segregated into distinct regions of the universe. It seems much more likely that they would have been created homogeneously and annihilated everywhere.

Given that the universe is dominated by matter, how did this imbalance arise? One answer could be that the asymmetry was built in. However, this is not a satisfying conclusion. Virtually any composition of the universe could be explained in this way, and it requires the imposition of initial conditions with no apparent rationale. The most attractive explanation of the matter/antimatter imbalance lies in an argument that starts with a symmetric universe that develops an imbalance through some observable mechanism some time after the Big Bang [7]. The Sakharov Criteria state the minimum conditions necessary for this asymmetry to develop from an initially symmetric universe. These criteria are listed below [5, 6].

1. Baryon non-conserving interactions occur.
2. CP invariance must be violated.
3. Statistical thermal equilibrium does not exist at the time that conditions 1 and 2 were able to operate.

It is beyond the scope of this thesis to discuss the Sakharov Criteria in detail. However, a very brief discussion of conditions 1 and 3 is in order here. The following sections will address only CP invariance violation.

The properties (except mass) of any particle can be completely described, according to the Standard Model, by the values of their *quantum numbers*. An example of a quantum number is electric charge. An electron has charge quantum number -1, a proton +1, a photon 0, a u quark +2/3, and so on. One fundamental law of interactions is that electric charge is conserved. The total charge of a system before interaction must be equal to the total charge after.

Another quantum number is *baryon number*. Baryons are three-quark bound states. Each baryon has baryon number +1, and antibaryons have baryon number -1. All other particles have baryon number 0. Baryon number has long been thought to be conserved in interactions, just like charge. The reason this appears to be the case is that if baryon number was not conserved, the proton (the least massive particle with baryon number +1) could decay into lighter particles with baryon number 0 (say a positron and a neutrino). The consequence of this decay would be to make impossible the existence of stable atoms. All of the protons in the universe would have long ago decayed away to lighter particles.

The dominance of matter over antimatter in the universe is tantamount to the universe having a positive baryon number. Again, the following arguments will be based on the assumption that the universe began with baryon number 0 and developed an imbalance as seen today. This implies that baryon non-conserving interactions must have taken place at some point in the evolution of the universe. It is postulated that very early in the history of the universe, the temperature being in excess of 10^{28} K, the weak and strong interactions were unified and this unified force was mediated by another gauge boson (call it X, for convenience). These X bosons were very massive and could decay via baryon number violating interactions. Once the temperature of the universe dropped below this threshold, the strong and weak interactions decoupled and no more of these X's were created. Eventually, all of the X's decayed away in their baryon non-conserving interactions. This requires that statistical thermal equilibrium did not apply at this point in the history of the universe.

Postulating the existence of the X boson is not sufficient to explain the baryon asymmetry of the universe, however. Symmetry arguments made previously would predict that equal numbers of its antiparticle would be produced and decay via non-antibaryon conserving interactions. Later, it will be shown that CP violation allows asymmetry in the decays of particles and their antiparticles. These two mechanisms, baryon non-conserving interactions and CP violation, acting together in a non-equilibrium situation might have been sufficient to cause the dominance of matter over antimatter in the universe.

It should be noted that in fact the asymmetry need only be small. A one in one billion excess of baryons over antibaryons in the early universe would be sufficient to result in the matter dominated universe seen today.

1.3 CP Violation

The charge operator, C, which takes particles into antiparticles and the parity operator, P, which results in space inversion, are invariant in both the strong and electromagnetic interactions. It was assumed until the late 1950's that C, P, and T (the time reversal operator) were individually conserved in all interactions. In the case of parity, this symmetry would mean that if a particular interaction takes place, its mirror image must also take place with equal likelihood. However, large violations of P were seen in weak interactions, most notably by C.S. Wu in the famous ^{60}Co experiment [8]. The electrons created in the β decay of ^{60}Co are emitted in a preferential direction. In fact, it is now said that charged current weak interactions violate parity maximally, due to the coupling of the $W^{\pm}$ exclusively to lefthanded fermions (there is no mirror symmetry) as stated in Section 1.1.

Next, it was postulated that C and P operating together were conserved. This transformation takes a physical particle state into a physical antiparticle state. Consequently invariance under CP implies a particle-antiparticle symmetry in nature. As mentioned in Section 1.2, however, the universe is dominated by matter. This observation requires that CP violating interactions take place.

1.3.1 The K Mesons

CP violation has been observed in the neutral K system. Both K^0 (quark content: $\bar{s}d$) and $\overline{K^0}$ ($s\bar{d}$) are seen to decay into $\pi^+\pi^-$ and into $\pi^+\pi^-\pi^0$ as shown in Figure 1.2 ($\pi^+ = u\bar{d}$, $\pi^- = \bar{u}d$ and $\pi^0 =$ a mixture of $u\bar{u}$ and $d\bar{d}$). Since they share decay channels they can mix through the weak interaction. In other words, K^0's can change into $\overline{K^0}$'s via an exchange of $W^{\pm}$ bosons. The lowest order diagram of this oscillation through pions is shown in Figure 1.3a. This "box diagram" is called a virtual process while the

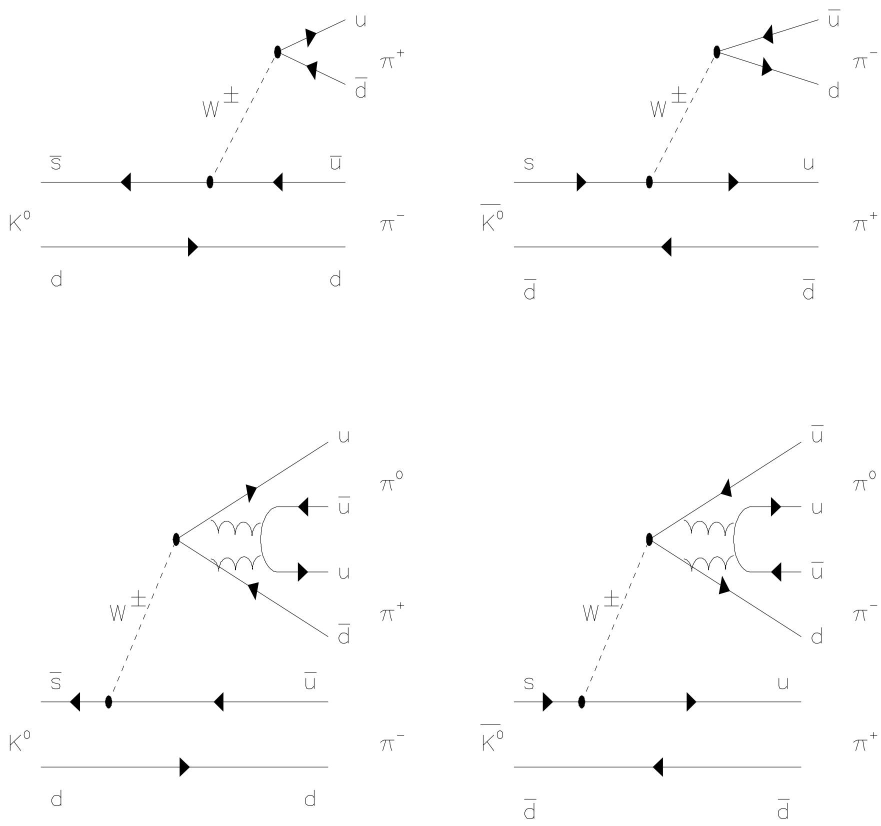

Figure 1.2: The decay of both the K^0 and $\overline{K^0}$ particles to two and three pions.

oscillation shown in Figure 1.3b is called a real process since the the intermediate state of pions can be seen in nature (remember that a single u quark is never seen due its colour charge). The result is that through weak decays K^0's and $\overline{K^0}$'s cease to be orthogonal states (ie. they cease to be distinct particles). While they are eigenstates of the strong interaction, the same cannot be said for the weak [9].

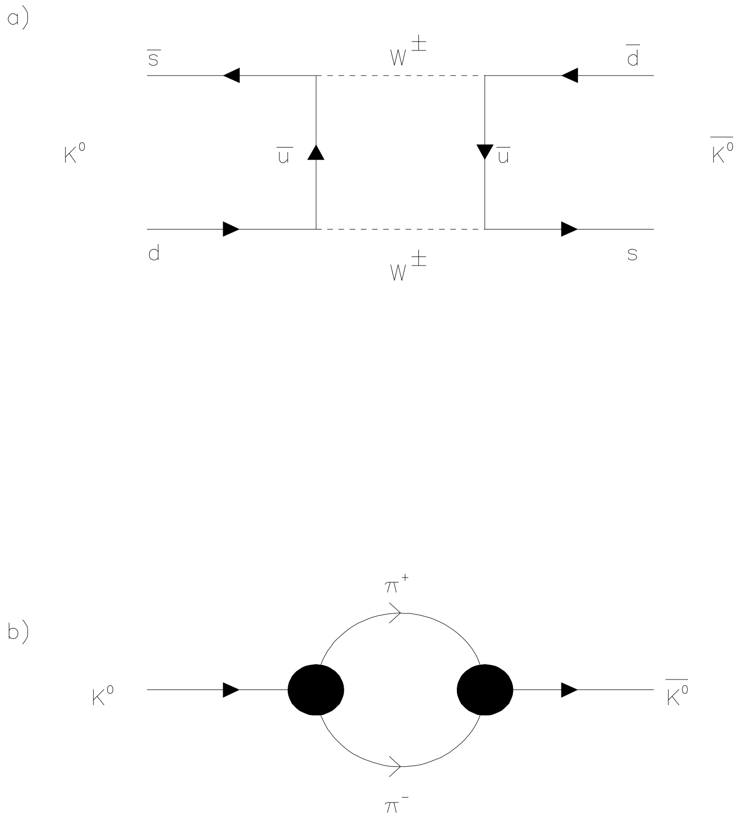

Figure 1.3: a)K^0's oscillate into $\overline{K^0}$'s via the exchange of $W^{\pm}$ bosons and, b) via a real intermediate state of pions.

The neutral kaons can be considered as linear combinations of two weak eigenstates, K_1^0 and K_2^0 as follows:

$$\begin{aligned} |K^0\rangle &= \tfrac{1}{\sqrt{2}}(|K_1^0\rangle + |K_2^0\rangle) \\ |\overline{K^0}\rangle &= -\tfrac{1}{\sqrt{2}}(|K_1^0\rangle - |K_2^0\rangle) \end{aligned} \tag{1.4}$$

The states $|K_1^0\rangle$ and $|K_2^0\rangle$ would be CP eigenstates with eigenvalues +1 and -1 respectively. Consequently, each of these states would be responsible for specific decays of neutral kaons, for example:

$$\begin{aligned} K_1^0 &\rightarrow \pi^+ + \pi^- \\ K_2^0 &\rightarrow \pi^+ + \pi^- + \pi^0 \end{aligned} \tag{1.5}$$

since $\pi^+\pi^-$ is a CP eigenstate with eigenvalue +1, while $\pi^+\pi^-\pi^0$ has eigenvalue -1. The phase space of the two-body decay would be much larger than that of the three body decay so the state $|K_2^0\rangle$ would have a longer lifetime than $|K_1^0\rangle$. Most importantly, since these weak eigenstates are orthogonal, they would not have common decay channels. If CP is conserved in weak interactions, K_2^0 should never be seen to decay into a CP eigenstate with eigenvalue +1.

$$\begin{aligned} K_2^0 &\not\rightarrow \pi^0 + \pi^0 \\ K_2^0 &\not\rightarrow \pi^+ + \pi^- \end{aligned} \tag{1.6}$$

Two components of K^0 are indeed observed, one long-lived and one short-lived. However, the long-lived component is seen to decay into two pions with a branching ratio on the order of 2.3×10^{-3}. So, instead of K_1^0 and K_2^0, one constructs the following eigenstates of the neutral K system:

$$\begin{aligned} |K_S^0\rangle &= p|K^0\rangle + q|\overline{K^0}\rangle \\ |K_L^0\rangle &= p|K^0\rangle - q|\overline{K^0}\rangle \end{aligned} \tag{1.7}$$

CP violation in K^0-$\overline{K^0}$ gives:

$$\frac{q}{p} = \frac{1-\tilde{\epsilon}}{1+\tilde{\epsilon}} \tag{1.8}$$

Here, $\tilde{\epsilon}$ is a measure of CP violation in the K system. If CP violation did not occur in this system, $\tilde{\epsilon} = 0$ and $p = q = \frac{1}{\sqrt{2}}$.

To summarize, CP violation is manifested in the neutral K system by the existence of two physical particles (K_S^0 and K_L^0) with very similar masses, but much different decay rates, which both decay into two pion and three pion CP eigenstates (although not in equal proportions). It is shown that CP violation occurs, but more detail on its possible inclusion in the Standard Model requires further information. This information can be obtained through the study of the B meson system, which is shown in the next section.

1.3.2 The B Mesons

In order to understand why the B meson system is expected to be an excellent source for the study of CP violation, it is necessary to look at the CKM matrix defined in Section 1.1 in more detail. The CKM matrix is unitary (ie. $VV^\dagger = 1$). Applying this constraint to the first and third columns of the matrix 1.2 gives the relationship:

$$V_{ud}V_{ub}^* + V_{cd}V_{cb}^* + V_{td}V_{tb}^* = 0 \tag{1.9}$$

The *unitary triangle*, shown in Figure 1.4a [10], is simply a geometric representation of Equation 1.9 in the complex plane. It should be noted that while the triangle shown here is referred to as *the* unitary triangle, the constraint of unitarity can be applied to all the other rows and columns of V resulting in a total of 6 unitary triangles.

The experimental measurements of the magnitudes of the elements of the CKM matrix given in Equation 1.3 show that $s_{12} \approx 0.22$, $s_{23} \approx s_{12}^2 \approx 0.05$ and $s_{13} \approx s_{12}^3 \approx 0.01$ which

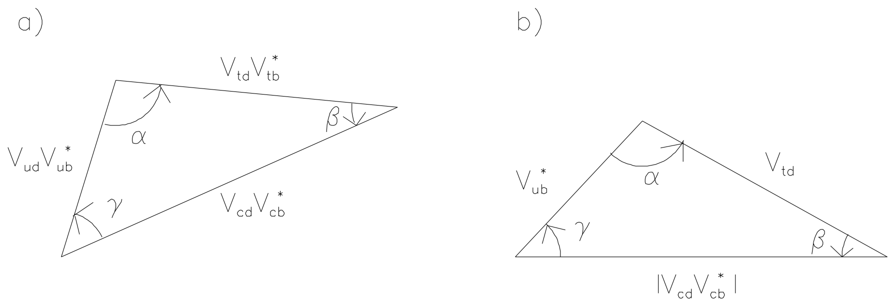

Figure 1.4: The "unitary triangle".

allows V to be represented, to a very good approximation, by:

$$V \approx \begin{pmatrix} 1 & s_{12} & s_{13}e^{-i\delta} \\ -s_{12} & 1 & s_{23} \\ s_{12}s_{23} - s_{13}e^{i\delta} & -s_{23} & 1 \end{pmatrix} \tag{1.10}$$

Note that in the above parameterization, all of the elements of V are real except V_{ub} and V_{td}.

Using the parameterization 1.10, equation 1.9 becomes:

$$V_{ub}^* + V_{td} \cong -V_{cb}^* V_{cd} \tag{1.11}$$

Since, according to the parameterization above, the elements V_{cb} and V_{cd} are real (or very nearly), the unitary triangle will have one side along the real axis, as shown in Figure 1.4b.

The angles α, β, and γ result from a non-zero phase, δ, in the CKM matrix. This phase incorporates CP violation into the Standard Model. If CP violation did not occur, all of the angles of the unitary triangle would be zero. If the angles do not add up to π radians, interactions are occuring that are not explained by the Standard Model.

If one notes that $Im(\frac{z}{z^*}) = \sin(2\theta)$ and $z = Re^{i\theta}$, it follows from Figure 1.4a that:

$$Im\left(\frac{V_{ub}V_{ud}^*}{V_{ub}^*V_{ud}}\frac{V_{td}V_{tb}^*}{V_{td}^*V_{tb}}\right) = \sin 2\alpha \tag{1.12}$$

$$Im\left(\frac{V_{td}V_{tb}^*}{V_{td}^*V_{tb}}\frac{V_{cd}^*V_{cb}}{V_{cd}V_{cb}^*}\right) = -\sin 2\beta \tag{1.13}$$

$$Im\left(\frac{V_{ud}V_{ub}^*}{V_{ud}^*V_{ub}}\frac{V_{cd}^*V_{cb}}{V_{cd}V_{cb}^*}\right) = \sin 2\gamma \tag{1.14}$$

The quantities 2α, 2β and 2γ can be measured through the study of time-dependent, CP violating asymmetries in decays of neutral B mesons [4].

It is useful to define several quantities for the discussion of time-dependent, CP violating asymmetries. The B particles produced in the e^+/e^- collision with a specific quark content are denoted by $B^0 \equiv \bar{b}d$ and $\overline{B^0} \equiv b\bar{d}$. These are not necessarily mass eigenstates, denoted by B_1 and B_2, nor are they CP eigenstates, $B_+ \equiv B^0 + \bar{B}^0$ and $B_- \equiv B^0 - \bar{B}^0$. B_+ and B_- are somewhat analogous to K_1 and K_2 in Section 1.3.1 as CP eigenstates with eigenvalues +1 and -1 respectively.

The Hamiltonian for the neutral B system is given by:

$$H = \begin{pmatrix} M & M_{12} \\ M_{12}^* & M \end{pmatrix} - \frac{i}{2} \begin{pmatrix} \Gamma & \Gamma_{12} \\ \Gamma_{12}^* & \Gamma \end{pmatrix} \tag{1.15}$$

where the first matrix is the *mass matrix* and the second matrix is the *decay matrix* [10].

The mass matrix describes processes involving virtual intermediate states that do not lead to the decay of the meson. The off-diagonal elements are dominated (in the Standard Model) by $\overline{B^0} \leftrightarrow B^0$ mixing via two virtual top quarks. The diagram for such mixing is shown in Figure 1.5.

The off diagonal elements are therefore proportional to the quark mixing matrix elements at the four vertices:

$$M_{12} \propto (V_{tb} V_{td}^*)^2 \tag{1.16}$$

for the B_d system. A similar argument results in:

$$M_{12}^s \propto (V_{tb} V_{ts}^*)^2 \tag{1.17}$$

for the B_s^0 system ($B_s^0 = \bar{b}s$).

The decay matrix describes processes with real intermediate states which can result in the decay of the meson. Here again, the off-diagonal elements are due to $\overline{B^0} \leftrightarrow B^0$ mixing. The dominant decays of B^0 are to final states containing a $\bar{c}$ ($B^0 \rightarrow X l \nu_l$, branching ratio $= 9.5 \pm 1.6\%$ where X is dominated by anticharm) and the $\overline{B^0}$ to final states containing a c quark. This means that, unlike the K system mixing via real pions, the real states accessible to both B^0 and $\overline{B^0}$ are highly Cabibbo suppressed. Therefore,

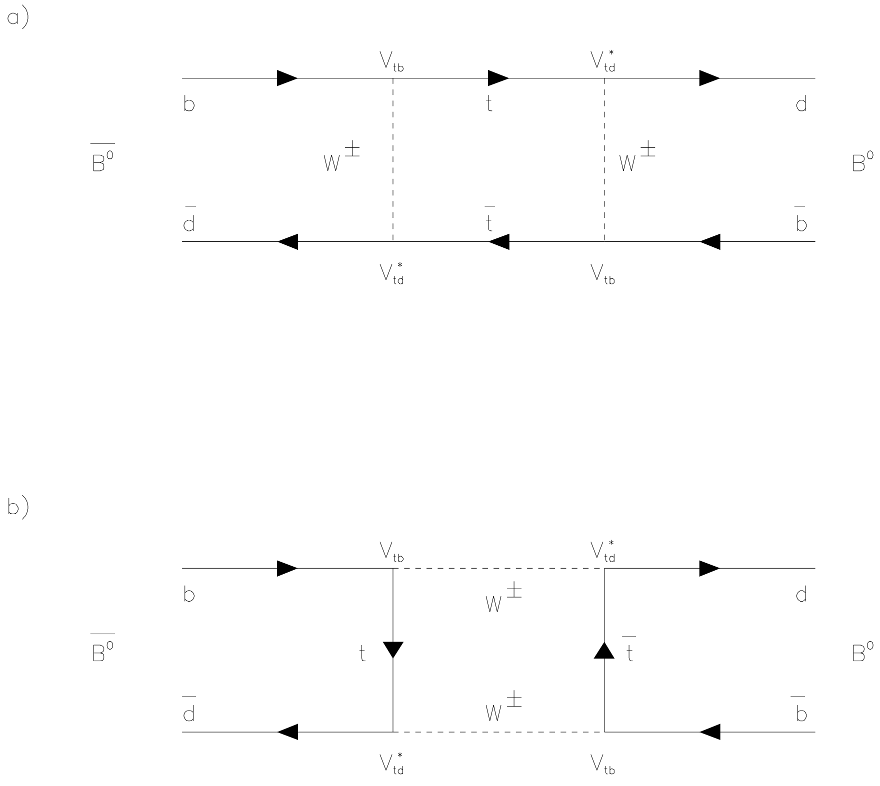

Figure 1.5: $\overline{B^0}$ - B^0 mixing via two virtual top quarks.

it is expected that:

$$|\Gamma_{12}| \ll |M_{12}| \tag{1.18}$$

The eigenvectors of H are B_1 and B_2, the mass eigenstates:

$$\begin{aligned} |B_1\rangle &= p|B^0\rangle + q|\overline{B^0}\rangle \\ |B_2\rangle &= p|B^0\rangle - q|\overline{B^0}\rangle \end{aligned} \tag{1.19}$$

(compare to Equation 1.7) and

$$\frac{q}{p} = \sqrt{\frac{M^*_{12} - i\Gamma^*_{12}/2}{M_{12} - i\Gamma_{12}/2}} \tag{1.20}$$

Using the approximation in Equation 1.18,

$$\frac{q}{p} \cong \sqrt{\frac{M^*_{12}}{M_{12}}} \Rightarrow \left|\frac{q}{p}\right| \cong 1 \tag{1.21}$$

The eigenvalues corresponding to the eigenvectors B_1 and B_2 are $m_1 - \frac{i}{2}\Gamma_1$ and $m_2 - \frac{i}{2}\Gamma_2$ where:

$$\begin{aligned} m_{1,2} &\equiv M \pm ReQ, \\ \Gamma_{1,2} &\equiv \Gamma \pm ImQ \\ Q &\equiv \sqrt{(M^*_{12} - \tfrac{i}{2}\Gamma^*_{12})(M_{12} - \tfrac{i}{2}\Gamma_{12})} \end{aligned} \tag{1.22}$$

From Equation 1.18 it is clear that:

$$\Delta\Gamma \ll \Delta m \tag{1.23}$$

These quantities ($\Delta\Gamma$ and Δm) are measurable [4, 10]. They are simply the difference in the decay rates and the masses of the physical B mesons. Note that the B meson system is opposite in this respect to the K meson system. In the case of the K mesons, the two physical particles K^0_L and K^0_S have almost identical masses, but very different lifetimes, while in the B system the masses are different and the lifetimes are expected to be very similar.

Since the physical states B^0 and $\overline{B^0}$ produced at $t = 0$ can mix, these states evolve in time. An initially pure B^0 develops a $\overline{B^0}$ component. To further the discussion of CP violation, only decay to final states which are CP eigenstates (f_{CP}) accessible to both physical states, will be considered here. As previously mentioned, these decays are highly Cabibbo suppressed and therefore have extremely small branching ratios (10^{-3} to 10^{-5}).

The amplitude for a time-evolved B^0 or $\overline{B^0}$ to decay to f_{CP} is given by:

$$\begin{aligned}\langle f_{CP}|B^0_{phys}(t)\rangle &= f_+(t)\langle f_{CP}|B^0\rangle + \tfrac{q}{p} f_-(t)\langle f_{CP}|\overline{B^0}\rangle \\ \langle f_{CP}|\overline{B^0}_{phys}(t)\rangle &= \tfrac{p}{q} f_-(t)\langle f_{CP}|B^0\rangle + f_+(t)\langle f_{CP}|\overline{B^0}\rangle\end{aligned} \tag{1.24}$$

where f_+ and f_- are defined as follows:

$$\begin{aligned}f_+(t) &\equiv e^{-imt}e^{-\Gamma t/2}\cos\tfrac{\Delta mt}{2} \\ f_-(t) &\equiv e^{-imt}e^{-\Gamma t/2} i \sin\tfrac{\Delta mt}{2}\end{aligned} \tag{1.25}$$

and m and Γ are the mean mass and decay rate of the physical B mesons respectively. The time-dependent rate for an initially pure physical state to decay into a final CP eigenstate, then, is found by multiplying the equations in 1.24 by their complex conjugates:

$$\begin{aligned}\Gamma(B^0_{phys}(t) \to f_{CP}) &= |\langle f_{CP}|B^0\rangle|^2 e^{-\Gamma t} \times \{\cos^2\tfrac{\Delta mt}{2} + |\lambda|^2 \sin^2\tfrac{\Delta mt}{2} - 2Im\lambda \sin\tfrac{\Delta mt}{2}\cos\tfrac{\Delta mt}{2}\} \\ \Gamma(\overline{B^0}_{phys}(t) \to f_{CP}) &= |\langle f_{CP}|\overline{B^0}\rangle|^2 e^{-\Gamma t} \times \{\cos^2\tfrac{\Delta mt}{2} + \tfrac{1}{|\lambda|^2} \sin^2\tfrac{\Delta mt}{2} - 2Im\lambda^{-1} \sin\tfrac{\Delta mt}{2}\cos\tfrac{\Delta mt}{2}\}\end{aligned} \tag{1.26}$$

where λ is defined as:

$$\lambda \equiv \frac{q}{p}\frac{\langle f_{CP}|\overline{B^0}\rangle}{\langle f_{CP}|B^0\rangle} \tag{1.27}$$

Using Equation 1.21 and noting that if a single weak-decay diagram dominates:

$$\left|\frac{\langle f_{CP}|\overline{B^0}\rangle}{\langle f_{CP}|B^0\rangle}\right| \cong 1 \tag{1.28}$$

and it follows that

$$|\lambda| \equiv \left|\frac{q}{p}\right|\left|\frac{\langle f_{CP}|\overline{B^0}\rangle}{\langle f_{CP}|B^0\rangle}\right| \cong 1 \tag{1.29}$$

In other words, in the B meson system, λ is pure phase ($\lambda = e^{i\phi}$) and $Im\lambda = -Im\lambda^{-1}$.

In the end, the equations in 1.26 simplify to (for $\Delta m \rightarrow 0$):

$$\begin{aligned} \Gamma(B^0_{phys}(t) \rightarrow f_{CP}) &\cong |\langle f_{CP}|B^0\rangle|^2 e^{-\Gamma t}\{1 - Im\lambda \sin\Delta mt\} \\ \Gamma(\overline{B^0}_{phys}(t) \rightarrow f_{CP}) &\cong |\langle f_{CP}|\overline{B^0}\rangle|^2 e^{-\Gamma t}\{1 + Im\lambda \sin\Delta mt\} \end{aligned} \tag{1.30}$$

The time-evolved, CP-violating asymmetry in the decay rate of an initially pure B^0 state to a CP eigenstate, compared to that of an initially pure $\overline{B^0}$ is given by:

$$A(B \rightarrow f_{CP}) \equiv \frac{\Gamma[\overline{B^0}_{phys}(t) \rightarrow f_{CP}] - \Gamma[B^0_{phys}(t) \rightarrow f_{CP}]}{\Gamma[\overline{B^0}_{phys}(t) \rightarrow f_{CP}] + \Gamma[B^0_{phys}(t) \rightarrow f_{CP}]} = Im\lambda \sin\Delta mt \tag{1.31}$$

Recalling Equations 1.16, 1.21 and 1.27, λ can be written as:

$$\begin{aligned} \lambda_d &= \frac{V^*_{tb}V_{td}}{V_{tb}V^*_{td}} \frac{\langle f_{CP}|\overline{B^0_d}\rangle}{\langle f_{CP}|B^0_d\rangle} \\ \lambda_s &= \frac{V^*_{tb}V_{ts}}{V_{tb}V^*_{ts}} \frac{\langle f_{CP}|\overline{B^0_s}\rangle}{\langle f_{CP}|B^0_s\rangle} \end{aligned} \tag{1.32}$$

It is now possible to see how the study of specific decays of neutral B mesons to CP eigenstates will enable the precise measurement of the angles of the unitary triangle.

The decay $B \rightarrow \pi^+\pi^-$ is shown in Figure 1.6a. The amplitude of this decay is proportional to $V^*_{ub}V_{ud}$. Therefore:

$$\lambda = \frac{V^*_{tb}V_{td}}{V_{tb}V^*_{td}} \frac{V_{ub}V^*_{ud}}{V^*_{ub}V_{ud}} \tag{1.33}$$

Since V_{tb} is nearly unity as is V_{ud}, and from 1.12:

$$Im\lambda = Im\frac{V^*_{tb}V_{td}}{V_{tb}V^*_{td}} \frac{V_{ub}V^*_{ud}}{V^*_{ub}V_{ud}} = \sin 2\alpha \tag{1.34}$$

It follows that the time-dependent asymmetry for $B \rightarrow \pi^+\pi^-$ is:

$$A(B \rightarrow \pi^+\pi^-) = Im\lambda \sin\Delta mt = \sin 2\alpha \sin\Delta mt \tag{1.35}$$

Next, Figure 1.6b shows the decay $B \rightarrow J/\psi K^0_S$. This is a more complicated decay in that the final state is a CP eigenstate only to the extent that K^0_S is a CP eigenstate.

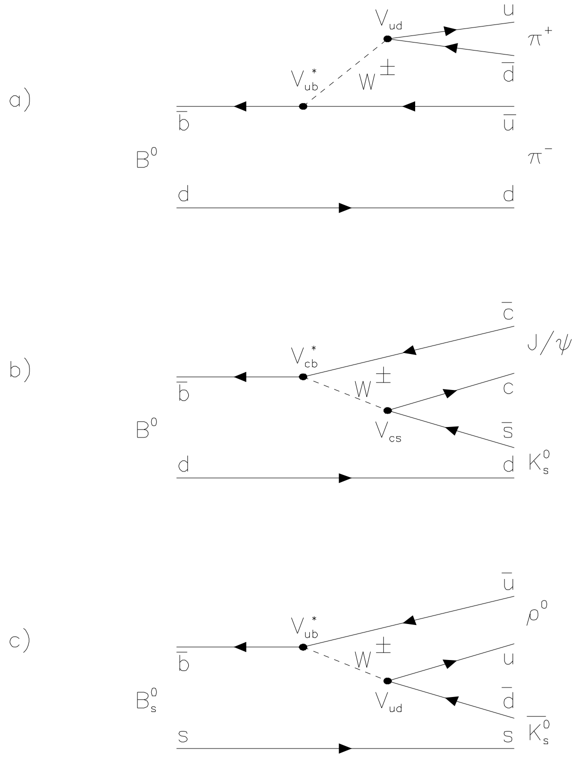

Figure 1.6: Three decay modes of B^0 to a CP eigenstate.

A factor $\frac{q}{p}$ arising from K^0- $\overline{K^0}$ mixing is included (see Figure 1.3) in the equation for λ:

$$\lambda = \frac{V_{tb}^* V_{td}}{V_{tb} V_{td}^*} \frac{V_{cb} V_{cs}^*}{V_{cb}^* V_{cs}} \frac{V_{cd}^* V_{cs}}{V_{cd} V_{cs}^*} = \frac{V_{tb}^* V_{td}}{V_{tb} V_{td}^*} \frac{V_{cb} V_{cd}^*}{V_{cb}^* V_{cd}} \tag{1.36}$$

Using the parameterization 1.10 this simplifies so that:

$$Im\lambda = Im \frac{V_{tb}^* V_{td}}{V_{tb} V_{td}^*} \frac{V_{cb} V_{cd}^*}{V_{cb}^* V_{cd}} = -\sin 2\beta \tag{1.37}$$

and the time-dependent asymmetry for $B \to J/\psi K_S^0$ is:

$$A(B \to J/\psi K_S^0) = -\sin 2\beta \sin \Delta m t \tag{1.38}$$

The last decay shown in Figure 1.6 is $B_s \to \rho K_S^0$. Again a term for K^0- $\overline{K^0}$ mixing is included in λ giving:

$$\lambda = \frac{V_{tb}^* V_{td}}{V_{tb} V_{td}^*} \frac{V_{ub} V_{ud}^*}{V_{ub}^* V_{ud}} \frac{V_{cd}^* V_{cs}}{V_{cd} V_{cs}^*} \tag{1.39}$$

and therefore:

$$Im\lambda = Im \frac{V_{tb}^* V_{td}}{V_{tb} V_{td}^*} \frac{V_{ub} V_{ud}^*}{V_{ub}^* V_{ud}} \frac{V_{cd}^* V_{cs}}{V_{cd} V_{cs}^*} = -\sin 2\gamma \tag{1.40}$$

and

$$A(B_s \to \rho K_S^0) = -\sin 2\gamma \sin \Delta m t \tag{1.41}$$

Other decay modes of interest in the study of time-evolved CP-violating asymmetries are listed in Table 1.1.

The decays of the neutral B meson system into final CP eigenstates allow precise measurement of the angles of the unitary triangle (and therefore good measure of CP violation) by measuring the time-dependent asymmetries. All that remains is the measurements themselves. There are three basic experimental requirements to measure the time-dependent asymmetries:

1. To produce B mesons.

2. To reconstruct B meson decays to CP eigenstates.

Table 1.1: More decay modes of the neutral B mesons.

Quark subprocess	Decay Mode	$Im\lambda$
$\bar{b} \to \bar{c} + c\bar{s},\ \bar{c} + c\bar{d},\ \bar{s}$	$B_d \to \psi K_S,\ \chi K_S,\ \phi K_S,\ \eta_c K_S,$ $\omega K_S,\ \rho K_S,\ D^+D^-,\ \overline{D^0}D^0,$ $\psi K_L,\ \phi K_L,\ \rho K_L,$	$-\sin(2\beta)$
$\bar{b} \to \bar{u} + u\bar{d}$	$B_d \to \pi^+\pi^-,\ \bar{p}p,\ \rho\pi^0,\ \omega\pi^0,\ \pi^0\pi^0$	$\sin(2\alpha)$
$\bar{b} \to \bar{u} + u\bar{d}$	$B_s \to \rho K_S,\ \omega K_S,\ \rho K_L,\ \omega K_L$	$-\sin(2\gamma)$
$\bar{b} \to \bar{c} + c\bar{s},\ \bar{c} + c\bar{d}$	$B_s \to \psi\phi,\ \eta_c\phi,\ \psi K_S$	$2\left\lvert\frac{V_{us}V_{ub}}{V_{ud}V_{cb}}\right\rvert \sin\gamma$

3. To determine the bottom-flavour (quark content b or $\bar{b}$) of the decaying B meson at $t = 0$ and to measure the decay time t.

The first requirement can be fulfilled in many ways. Large numbers of B mesons are produced at hadron colliders and fixed-target experiments. While the cross-section for production of $B^0/\overline{B^0}$ pairs is much higher for these types of experiments than at an e^+/e^- collider, it is a much smaller percentage of the total cross-section, so a very low signal-to-noise ratio results. The difficulty of picking the signal out of the background makes the ability to fulfill the other two requirements questionable. This leads to the conclusion that the best machine for B meson experiments is an e^+/e^- collider.

Using an e^+/e^- collider, the highest cross-sections for $B^0/\overline{B^0}$ production are found at the $\Upsilon(4S)$ *resonance* and at the Z^0 resonance. The $\Upsilon(4S)$ has quark content $b\bar{b}$. A resonance occurs when the energy of the colliding beams is equivalent to the mass of the particle produced, in this case 9.46 GeV. While the cross-section is highest for the Z^0 resonance, the $\Upsilon(4S)$ resonance is more attractive since the average number of charged tracks per $e^+e^- \to \Upsilon(4S) \to B^0\overline{B^0}$ event (ie. $e^+e^- \to q\bar{q}$ continuum) is much lower than for the Z^0 resonance. While there are other events produced at the $\Upsilon(4S)$ resonance, the signal-to-noise ratio of approximately one-to-three is better than at any other energy. Therefore, requirements 1 and 2 are best met by producing B mesons at an e^+/e^- collider running at the $\Upsilon(4S)$ resonance.

The branching ratio of the $\Upsilon(4S) \rightarrow B^0\overline{B^0}$ events as well as the lower resonance require that the e^+/e^- machine used have a very high luminosity. This is further reason to carefully consider the background rates. The machine and detector must be designed in such a way as to minimize the impact of luminosity related backgrounds, specifically synchrotron radiation, with serious attention paid to radiation hardness in a high-luminosity environment.

The necessity of identifying the flavour of the B meson at time $t = 0$ requires that the vertices of both the B^0 and $\overline{B^0}$ mesons can be resolved. This so-called "tagging" involves reconstructing the decay of one of the mesons produced in the $\Upsilon(4S)$ decay in order to determine whether it was a B^0 or $\overline{B^0}$. Once this is accomplished, the precise quark content of the other meson at $t = 0$ is known. This knowledge, combined with good time resolution for the decay and time-evolution of mixing, enables the decay of the second meson to be reconstructed and the CP violating parameters to be measured.

This criterion leads again to design considerations for both the machine and the detector. The PEP-II B-Factory has been designed asymmetrically with a 9 GeV electron beam and a 3.1 GeV positron beam. Particles produced by the colliding beams will therefore not be at rest in the lab frame. The result will be spatial separation of the decay vertices allowing for good resolution.

Detector requirements for good event tagging include excellent spatial resolution especially close to the interaction point (IP) to resolve vertices, as well as good particle identification and momentum resolution to separate out backgrounds from non-B decays. Further, multiple scattering from material in the detector must be minimized to attain the necessary momentum resolution. Finally, the asymmetry in beam energies results in the need to have solid angle coverage for tracking, particle identification and calorimetry to small angles in the forward (electron beam) direction.

The PEP-II B-Factory machine and *BaBar* detector at SLAC are currently being designed with the requirements of measuring the parameters of CP violation using the $B^0/\overline{B^0}$ system as benchmarks. Further discussion of the design considerations and specifics of the detector is given in later chapters.

Chapter 2

The PEP-II Machine and *BaBar* Detector

The B-Factory consists of three major components: the linear accelerator (Linac), the PEP-II Collider and the *BaBar* detector. This section is intended as a very brief overview of the various components. For a more complete discussion see [11, 12].

2.1 The Linac

Electrons produced by a heated filament are accelerated in SLAC's two-mile Linac to 9 GeV and injected into one of the PEP-II storage rings in a clockwise direction. The electron beam in the Linac is then aimed at a tungsten target to produce positrons. The positrons are accelerated to 3.1 GeV and injected into the other ring in a counter-clockwise direction. The charged particles are accelerated to velocities very close to the speed of light using electromagnetic fields in cavities along the accelerator.

2.2 The PEP-II Storage Rings

The storage rings are stacked in a single tunnel and cross at the interaction point (IP). After the IP the beams are redirected back into their respective rings. The result is that the beams actually cross at two points: the IP and a point 62 cm away from the IP. However, they do not collide at both points since they are separated horizontally with a bending magnet at the 62 cm point. Figure 2.7 shows the Linac and PEP-II storage rings.

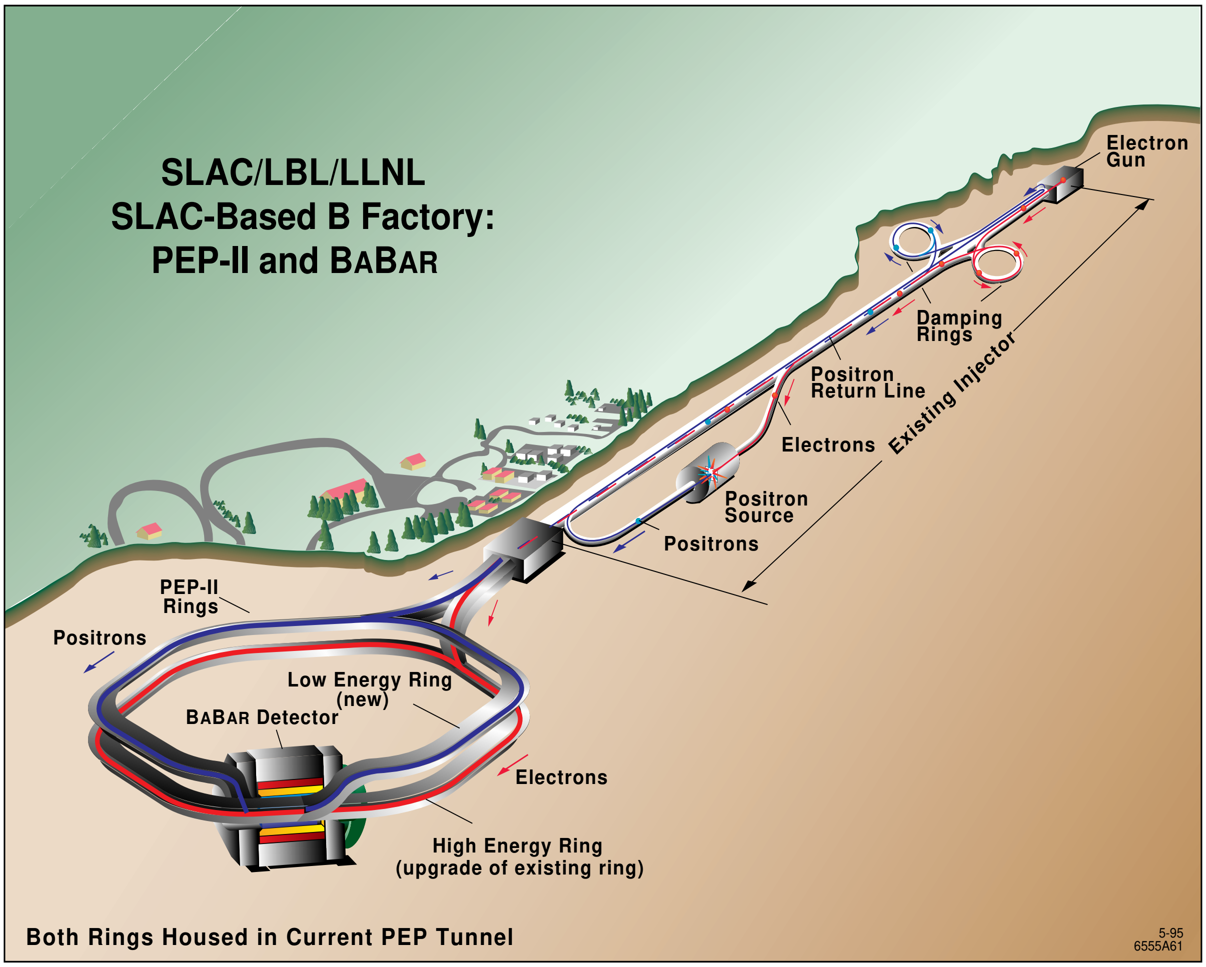

Figure 2.7: Schematic view of PEP-II complex on SLAC site.

The low branching ratios of the benchmark decays to be studied at the B-Factory require very high luminosity beams. The bunch crossing separation in PEP-II will be 4.3 ns. The beams must also be strongly focused near the IP to ensure a maximum collision rate and thus a high luminosity. This strong focusing is achieved by the placement of magnets very close to the IP in the interaction region (IR). The following section will discuss the IR in more detail as its design significantly impacts the study of background distributions in the drift chamber.

2.2.1 The Interaction Region

Figure 2.8 shows the PEP-II interaction region in detail. The low energy beam (LEB) enters from the lower right and exits through the upper left. The high energy beam (HEB) enters left and exits right. It is important to note that the scale of this figure is highly exaggerated in the vertical direction. Also note that the quadrupole magnet, Q1, and the dipole magnet, B1, are within the detector with all of B1 and some of Q1 to the inside of the drift chamber volume. The magnet B1 separates the beams horizontally before the second crossing point 62 cm downstream of the IP. Q1 focuses both the HEB and LEB. However, the LEB is off-axis in Q1 to maximize beam separation. Q2 focuses only the LEB with the HEB traversing a field free-region. Likewise, Q4 and Q5 focus only the HEB.

The Q1 and B1 magnets are within a 1.5 T magnetic field and therefore must be permanent or superconducting. It is possible for Q1 to be a superconducting magnet. However, space constraints would not allow the placement of a cryostat for B1. Consequently, both Q1 and B1 will be permanent, samarium cobalt magnets.

The beam pipe near the IP is a double-walled beryllium structure. The inner tube is 800 μm thick with a radius of 25 mm. The outer tube in 400 μm thick with a radius of 27 mm. Beryllium is chosen as the beam pipe material in order to reduce multiple scattering, and the tube is coated with 10 μm of gold to attenuate synchrotron radiation. The total beam pipe represents 0.6% of a radiation length.

There is also a support barrel within the detector volume on which the Q1 and B1 magnets, the IP beam pipe, and the vertex detector are assembled. The support barrel will be assembled and internally aligned before being inserted into the drift chamber. The end sections of the support barrel are made from stainless steel to support the Q1 magnet

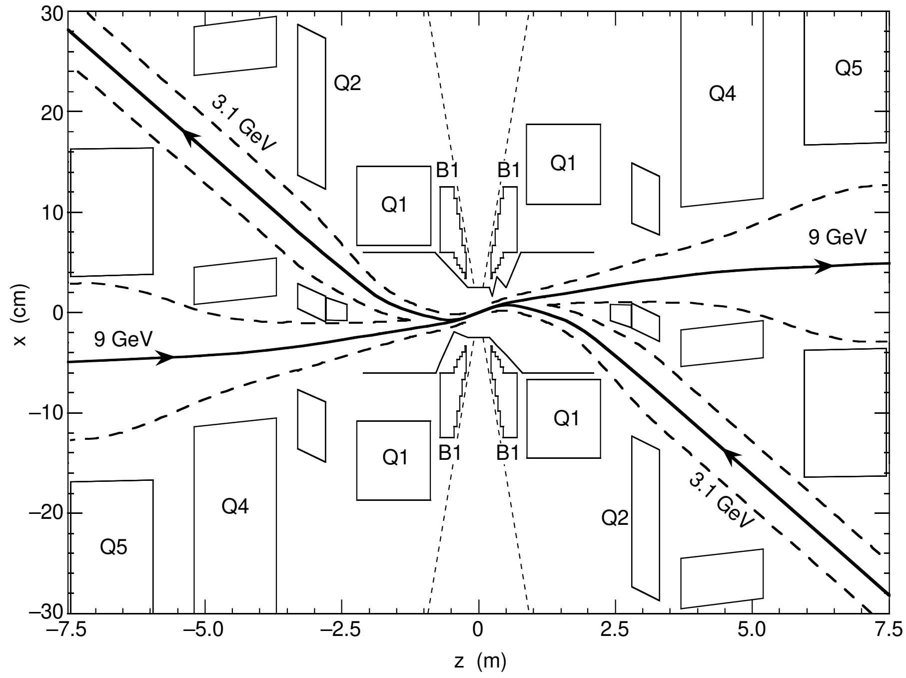

Figure 2.8: Plan view of the PEP-II interaction region. The vertical scale is highly exaggerated. The dashed lines represent the 300 mr detector acceptance cutoff.

assemblies. The barrel portion is constructed of a carbon fiber composite representing 0.005 radiation lengths (X_0). Figure 2.9 shows the support barrel and masks on the B1 magnet which are discussed later.

The location of the Q1 and B1 magnets so close to the IP is necessary for the separation and strong focusing of the beams. However, bending the beams with these magnets is also the source of a large synchrotron radiation flux (see Chapter 3). For this reason there are water-cooled beryllium masks inside the B1 magnet to prevent synchrotron radiation from striking the beam pipe.

Figure 2.10 shows the synchrotron radiation fans in the IR region. Aside from the synchrotron flux generated by beam separation and strong focusing within the detector

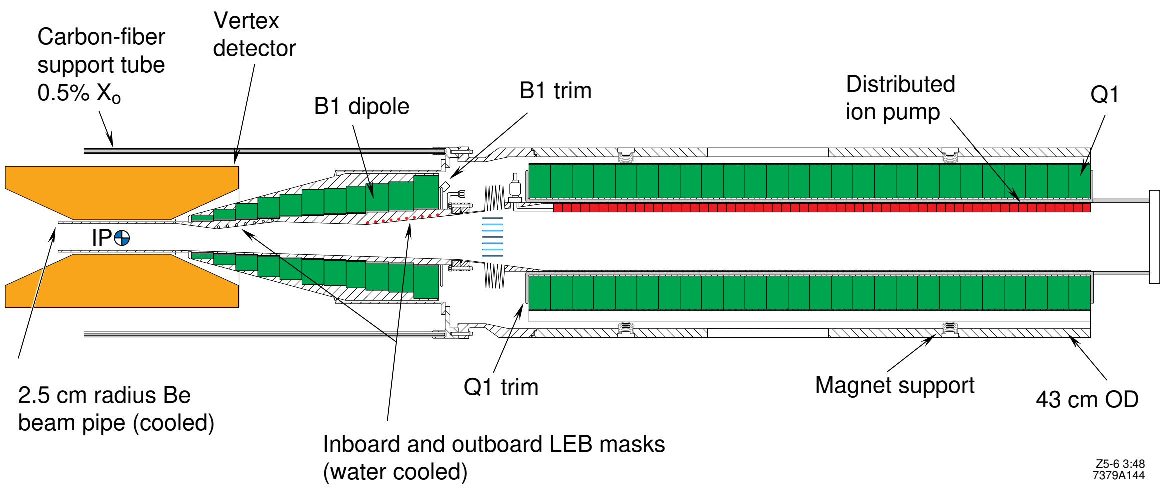

Figure 2.9: Support barrel for IR components inside the detector. Only one end is shown.

volume, other sources of radiation are: photons scattering off a mask tip, synchrotron photons generated far upstream of the IP and backscattered photons from downstream surfaces. With the addition of the masks to the IR design, the impact of synchrotron radiation backgrounds is minimized. In fact, while the high luminosity environment and bending within the detector volume would indicate greater difficulty with synchrotron radiation than in more conventional e^+/e^- machines, the masks eliminate the major sources of synchrotron radiation flux. The result is that synchrotron radiation is so small that it may be neglected in further background studies.

The IR having been designed to minimize synchrotron radiation backgrounds, the major source of backgrounds are Bremsstrahlung and Coulomb scattering of beam particles from residual gas molecules in the beam pipe. These can result in high energy beam particles and photons striking both the masks and the beam pipe near the IP. Electromagnetic showers caused by these collisions will result in both high detector occupancies and radiation damage. This effect is minimized by maintaining a very high vacuum in the beam pipe close to the IR. Studies have shown that it is possible to maintain pressures below 1 nTorr in regions from 3 to 40 m from the IP in either direction. However, due to space constraints, it is impossible to put pumps within the IR. For this reason, the pressure 3 m to either side of the IP is likely to exceed 1 nTorr.

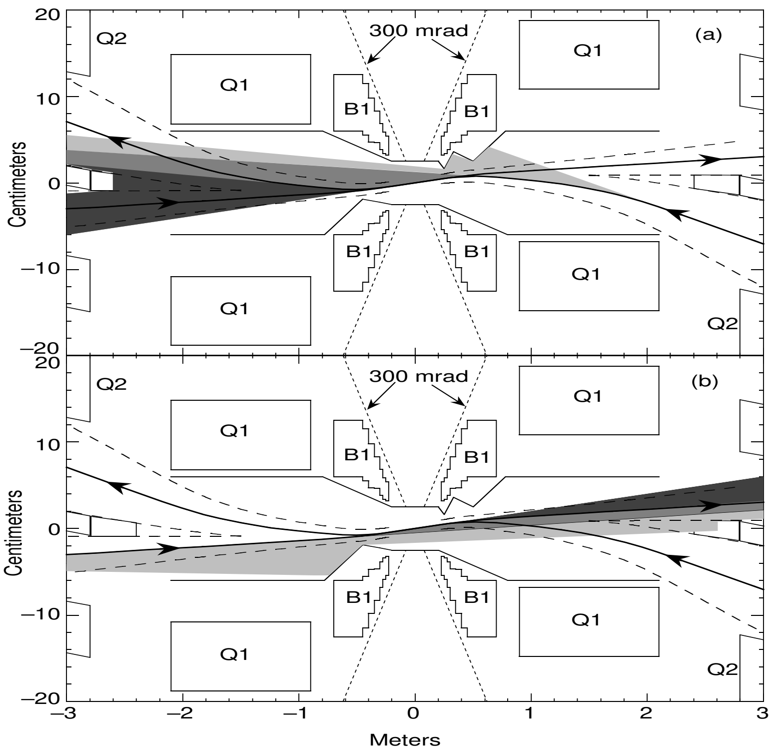

Figure 2.10: Synchrotron radiation beams for the low-energy (upper diagram) and high-energy (lower diagram) beams. The density of shading gives an indication of relative photon intensity from the various radiation fans.

2.3 The *BaBar* Detector

The *BaBar* detector is composed of five major components designed for precise measurements of parameters specific to CP violation in the B meson system. The major elements are a silicon strip vertex tracker, a drift chamber, a Cherenkov particle identification detector, a Cesium Iodide (CsI) electromagnetic calorimeter, and a magnet with instrumented flux return for muon detection. The components are concentric around the beam pipe and are offset in the forward direction. Figure 2.11 shows a cross-sectional view of the *BaBar* detector as the design was in 1995. Note that minor modifications continue to be made. For example, the endplates of the drift chamber are shown here as conical, but are now planned to be flat.

There are several issues that arise from factors discussed in Chapter 1 that must be considered in detector design. First, since the B system weak eigenstates have very similar (and short) lifetimes, the detector must have excellent spatial resolution near the interaction point in order to separate the vertices of B^0 and $\overline{B^0}$ decays. Second, low branching ratios for B decays result in background difficulties, both from non-B decays and from synchrotron and lost beam-particle backgrounds arising from the high luminosity required to produce enough events. The non-B decay backgrounds are excluded with excellent particle identification and momentum resolution. The synchrotron and lost beam-particle backgrounds must be minimized in the detector and accelerator design as discussed in the previous section. The need for precise momentum resolution, particularly for low momentum particles, necessitates minimization of multiple scattering. Third, the asymmetry in beam energies results in the need to have solid angle coverage for tracking, particle identification and calorimetry down to very near the beam pipe in the forward direction. Fourth, the electromagnetic calorimetry must be excellent particularly for reconstructing π^0's in B^0 decays. And finally, all detectors must be radiation

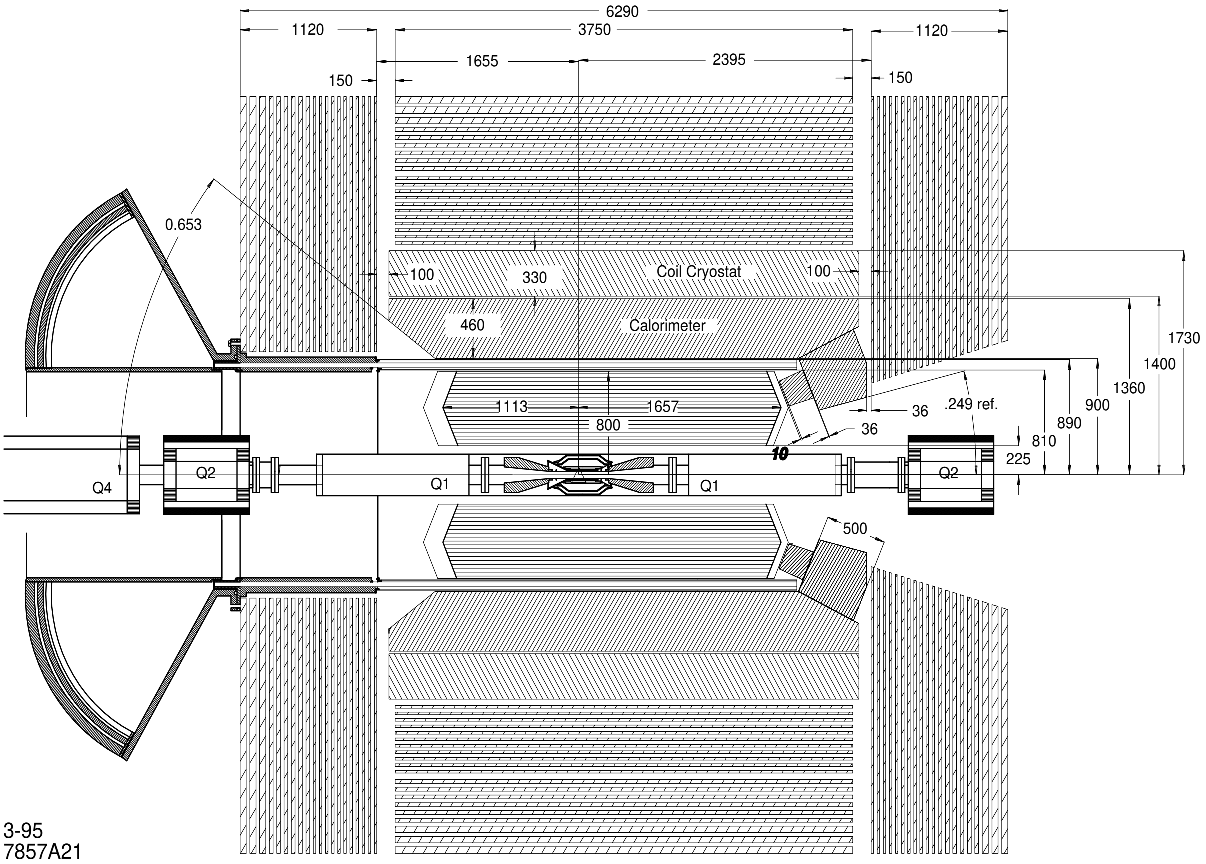

Figure 2.11: A cross-sectional view of the detector.

hard for long life in the high luminosity environment at *BaBar*.

While it is beyond the scope of this paper to discuss in detail the design of each detector component, a brief overview of each is presented here. A detailed treatment of the design of each component can be found in [12].

2.3.1 Silicon Vertex Detector

The silicon vertex tracker is located within the 20 cm radius of the carbon fiber support barrel. It and the drift chamber provide all the momentum and most of the tracking information for the detector. The vertex tracker must have excellent spatial resolution to determine the difference in decay times of the B^0 mesons. Additionally, it provides measurements of production angles. Also, low momentum particles loop in the 1.5 T magnetic field so tightly that they never enter the drift chamber. Such particles, with p_T (transverse momentum) between $\sim 40\ MeV/c$ and $\sim 100\ MeV/c$ are tracked only within the vertex tracker.

The location of the vertex tracker immediately surrounding the IP requires that the detector be reasonably radiation hard. Also, since it is located within the volume of other detectors, it requires low multiple scattering.

The vertex tracker is constructed from double-sided silicon strip detectors, arranged in five layers. The inner three layers have a barrel layout with the detectors parallel to the beam pipe. The outer two layers have a barrel layout in the central region, with wedge detectors in the forward and backward regions. Figures 2.12 and 2.13 show both a three-dimensional and cross-sectional view of the silicon vertex tracker.

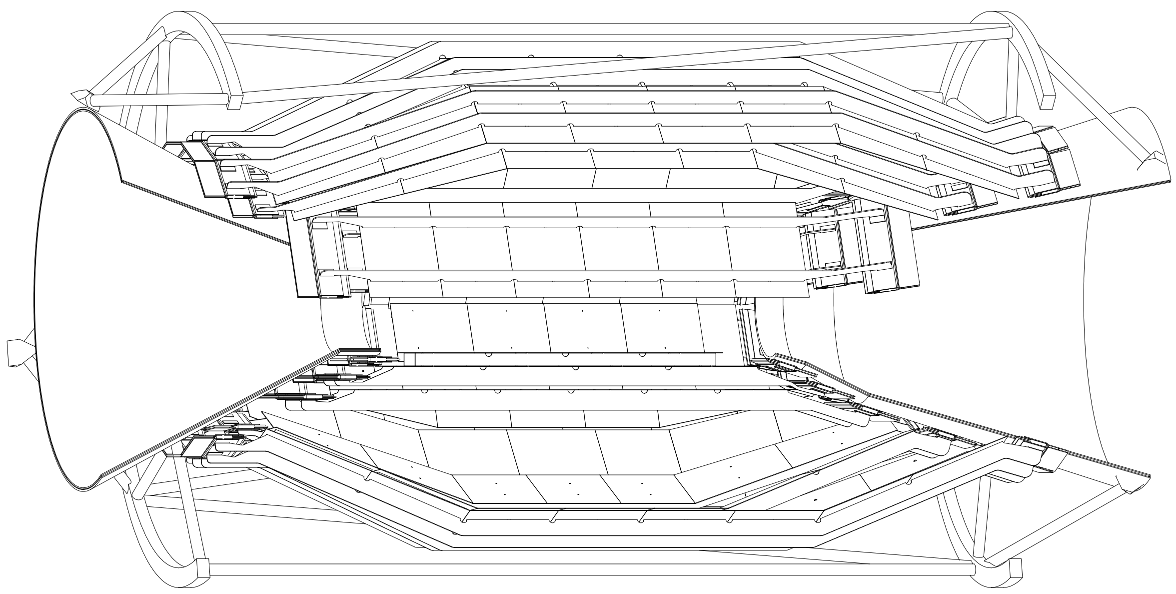

Figure 2.12: Three-dimensional cutaway view of the silicon vertex detector.

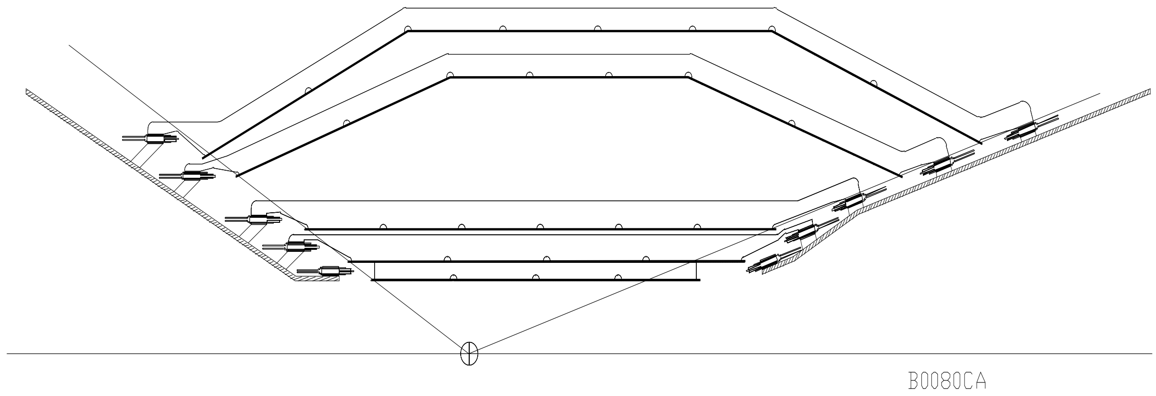

Figure 2.13: Cross-sectional view in a plane containing the beam axis.

The vertex tracker is somewhat larger than conventional silicon vertex detectors, with strips ranging in size from 95 mm $\times$ 39 mm (in ϕ and z respectively) in layer 1 to 241 mm $\times$ (35 $\rightarrow$ 52) mm in layer 5. The size is required in order for it to perform not only as a vertex tracker but also as a tracking device for low momentum particles.

The tracker achieves an intrinsic resolution of 25 μm at normal incidence, and a typical vertex (spatial) resolution of 60 $\rightarrow$ 75 μm depending on the species and momentum of the particle used to tag an event.

2.3.2 Drift Chamber

The second detector component is the drift chamber. Since measuring the parameters of CP violation in the B meson system requires that exclusive final states from B^0 and $\overline{B^0}$ decays be reconstructed efficiently and with high resolution, the drift chamber must provide good momentum resolution at all momenta, efficient reconstruction of even low momentum tracks, and good solid angle coverage. Its location inside the calorimeter requires that it not contribute significantly to multiple scattering. Additionally, it must provide particle identification through ionization loss for low momentum particles that don't reach the exterior particle identification component of the detector. Finally, the drift chamber provides one of the two major triggers of the experiment.

In order to achieve all of the above goals, a low-mass small-cell drift chamber has been designed for the BaBar detector. The small-cell arrangement will provide excellent tracking and energy loss resolution. The low-mass construction will minimize multiple scattering to improve momentum resolution while minimally degrading the performance of the particle identification and electromagnetic calorimeter components of the detector. Figure 2.14 shows a cross-sectional view of the 1995 drift chamber design.

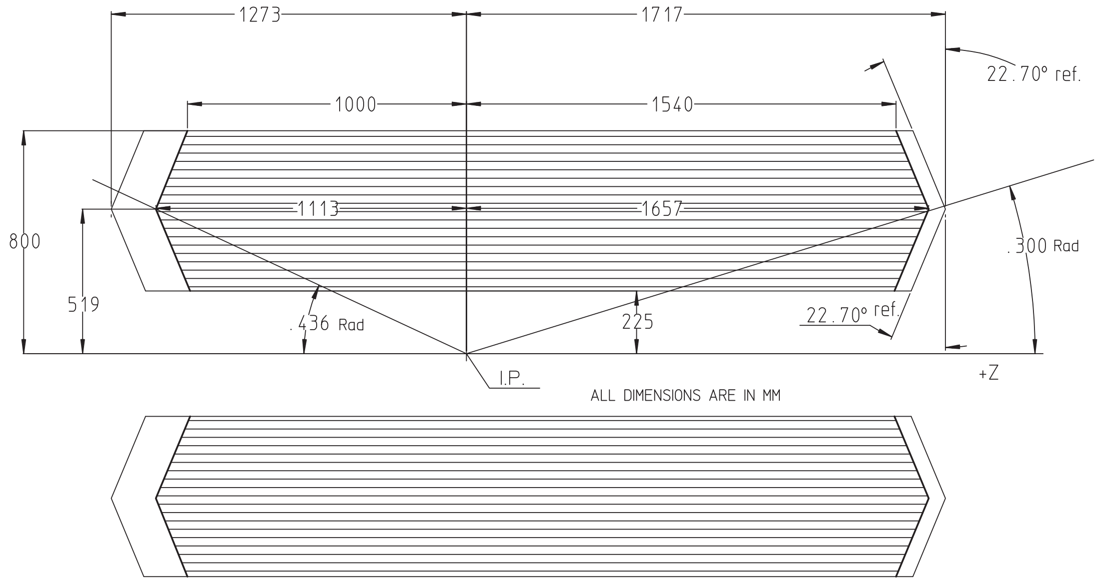

Figure 2.14: The drift chamber.

The drift chamber has an inner radius of 22.5 cm and an outer radius of 80 cm. It is 280 cm in length and bounded at the inner radius by the support tube, the outer radius by the particle identification detector, and in the forward region by the forward endcap of the electromagnetic calorimeter.

The volume of the drift chamber is filled with forty concentric layers of low-mass wires arranged in a small-cell configuration. Each cell consists of a gold plated tungsten wire anode (diameter 20 μm) surrounded by 80 μm and 120 μm gold plated aluminum field wires. The anode wires are also called sense wires as they provide the readout for the detector. The cells are rectangular in shape, 13 mm $\times$ 19 mm along the radial and azimuthal directions respectively. A voltage of +1.8 kV is applied to the sense wires while the field wires are maintained at ground and shape the electric field in the cell. This cell shape was chosen for the uniformity of the field produced in the cell while adding little mass to the system. With +1.8 kV applied, the avalanche gain is approximately 5×10^4.

The chamber is filled with a low atomic number gas mixture. The gas mixture is helium-based with additives to increase primary ionization and for quenching. The baseline gas mixture for the drift chamber is He:isobutane in a 80:20 combination. Other helium-based mixtures still under consideration include He:CO_2:isobutane (83:10:7).

A basic description of the operation of the drift chamber follows: as a charged particle traverses the drift chamber it ionizes the gas mixture molecules in its path. The ionized electrons then drift toward the anode. During this drift time, further gas molecules are ionized by the drifting electrons producing more electrons which drift toward the anode. This is known as the avalanche effect. As the electrons are accelerated in the field, more and more ionization occurs, producing more electrons. In the high field region near the sense wire, the avalanche effect occurs wherein a large number of electrons in a localized space are produced. The electrons are collected at the anode producing a pulse which is read out. Knowledge of which sense wire was struck, the drift velocity of electrons in the gas mixture, and the drift time of the electrons in the gas (start time determined by external trigger) allows for track reconstruction.

In the *BaBar* drift chamber, the layers of wires are arranged in superlayers. Superlayers consist of 4 layers which are all either axial or stereo. Axial superlayers run parallel to the beam line (defined as the z direction) and provide x, y information. Stereo superlayers are offset by a small angle (up to 3 degrees from end to end, depending on which layer is being considered). The stereo superlayers provide resolution in the z direction.

The total numbers of wires in the drift chamber are approximately 7104 sense wires and 28,768 field wires. All of the wires are strung tensed with a weight of 50g to reduce sag and better define the electric field produced in the cells. The maximum deflection due to gravity is 120μm at mid-length. The result is an axial load on the endplates of approximately 24,000kg. Consequently, the endplates must be manufactured in such a way as to sustain this load without flexing. However, since the endplates will be located within the calorimeter, they must also be of low mass. In order to maximize strength and minimize mass and construction complexity, a flat, aluminum endplate configuration is to be used. These represent approximately $0.14X_0$.

Due to the energy asymmetry of the beams, the drift chamber is offset in the forward (downstream for the electron beam) direction with a length of 166cm in the forward direction and 114cm in the backward direction.

The inner wall of the drift chamber is constructed of 1 mm of beryllium and carries 40% of the wire load. It also provides a gas seal and RF shield for the chamber. As such it must be able to support the pressure differential between the inside and outside of the chamber and it is designed to withstand 30mbar of overpressure.

The outer wall must be sufficiently strong to carry 60% of the axial load of the wires between the endplates. However, its large circumference allows this mechanical strength to be achieved with a 3.2 mm thick carbon fiber tube. This exceeds the nominal strength required to support the wire load and includes a safety factor for impact resistance.

All of the readout electronics and high voltage service boards are located on the backward (upstream) end of the drift chamber. Since there is no particle identification and limited calorimetry in this direction the significant number of radiation lengths represented by the electronics cards and cables is not problematic.

2.3.3 Particle Identification

Particle identification of both hadrons and leptons is crucial for the measurement of CP violation parameters in the B meson system. In particular, exclusive final states must be reconstructed and the quark content of the other B in the event must be tagged. Particle identification can be carried out for the most part by the drift chamber, electromagnetic calorimeter and instrumented flux return. However, a dedicated particle identification system is required to distinguish charged pions from kaons with momenta above 0.7 GeV/c and protons above 1.3 GeV/c. To this end, a ring-imaging Cherenkov detector has been designed for the barrel region of the detector immediately outside of the drift chamber.

All Cherenkov detectors operate on the same fundamental concept. Particles enter the detector medium, which has a different index of refraction than that of the medium outside the detector. The changed index of refraction results in the particle's speed exceeding that of light in the detector medium and the particle radiates photons in a characteristic cone distribution. The opening angle of the cone depends on the speed of the particle. Given the momentum of the particle (in *BABAR* this is determined in the drift chamber), the mass of the particle can be determined.

The DIRC (Detection of Internally Reflected Cherenkov light) is composed of 4.7 m long quartz bars oriented parallel to the z direction of the detector. The passage of a particle through the bars produces Cherenkov radiation. The photons produced are reflected internally and exit the bar at the backward end of the DIRC. The Cherenkov image is expanded from the end of the bar through a water-filled standoff region and is detected on a toroidal surface of photomultiplier tubes (PMT's). The PMT's are 1.125

in. in diameter and arranged in a close packed array 120cm from the ends of the quartz bars. There are mirrors at the forward end of each bar to reflect forward-going light back to the PMT's. The high optical quality of both the quartz bars and the forward mirrors preserve all angle information of the emitted Cherenkov light. Figure 2.15 shows a cross-sectional view of the DIRC.

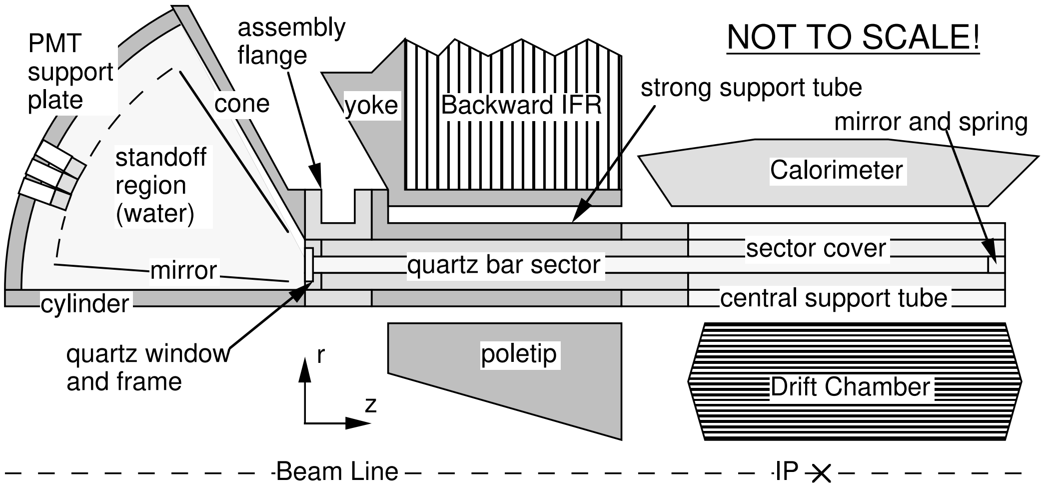

Figure 2.15: Schematic of the DIRC including support structures.

There is no dedicated particle identification system in the forward region, where the drift chamber, calorimeter and instrumented flux return will fulfill the particle identification requirements. Inclusion of a forward aerogel type of detector was proposed, but it was abandoned in the interest of minimizing the degradation of calorimetry for low-energy photons. No particle identification is needed in the backward region.

The DIRC system is ideal for the BaBar detector. The asymmetric energies of the beams produce a forward boost for high momentum particles. Since the angle of incidence is significantly off-normal, the particles have a longer path length in the quartz, increasing the light production and allowing the thickness of the quartz to be reduced. With this minimization of mass, the DIRC represents 0.18 X_0 for normal incidence. The small radial dimension also reduces the volume of the electromagnetic calorimeter [12].

2.3.4 Electromagnetic Calorimeter

The *BaBar* detector requires excellent calorimetry for several reasons. It is necessary to reconstruct CP eigenstates containing one or more π^0 decays. The small branching ratios of these CP eigenstates require high efficiency in detecting low-energy photons to make it possible to reconstruct final states containing several π^0's. Also, the calorimeter must provide lepton identification, again for tagging decays of CP eigenstates. A cesium iodide (CsI) crystal calorimeter has been designed to provide the necessary high resolution and efficiency.

The CsI calorimeter consists of a cylindrical barrel section, offset in the forward direction, with a forward conical endcap. The barrel has an inner radius of 90 cm and outer radius of 135.6 cm. The barrel is constructed of 250 μm thick carbon fiber composite compartments that house individual crystals. Each crystal is wrapped with a diffuse reflecting material on its sides and a reflector on its front face. The crystals are tapered along their lengths with the average area of the front faces being 4.8cm $\times$ 4.7cm and the back faces 6.1cm $\times$ 6.0cm. They vary in length in $0.5X_0$ steps from $17.5X_0$ in the forward part of the barrel and the endcap to $16.0X_0$ in the backward part of the barrel.

Photodiodes and preamplifier packages provide readout and are located at the outer end of each compartment. The choice of photodiodes as readout devices was made since readout must be accomplished in the 1.5 T magnetic field. The forward endcap is segmented vertically into two pieces, each of which can be removed separately allowing relatively easy access to the barrel end region. Figure 2.16 shows a cross-sectional view of the CsI calorimeter.

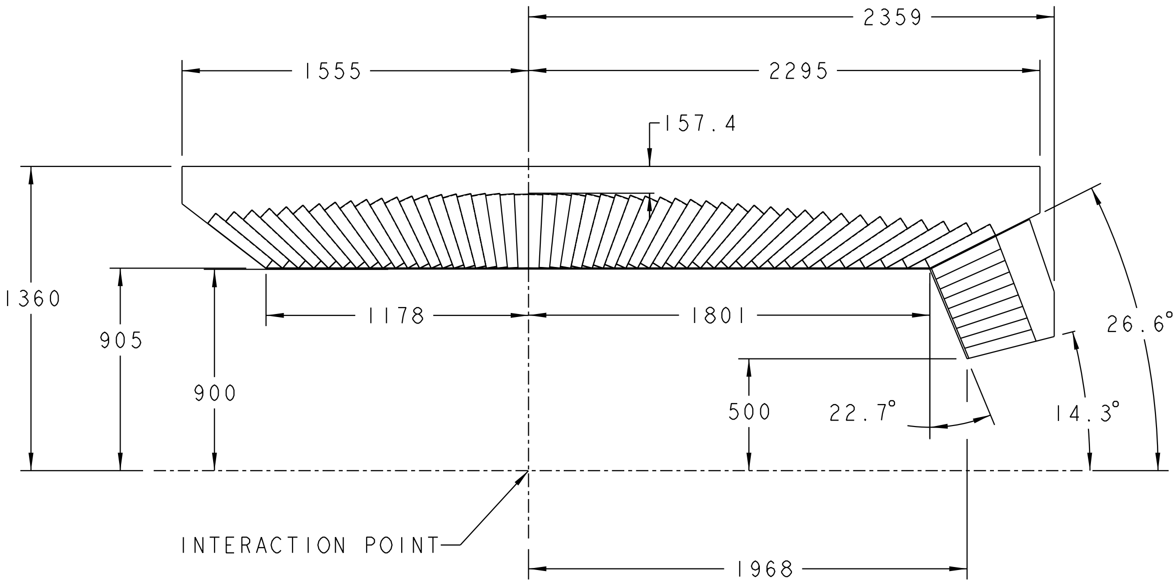

Figure 2.16: Side view showing dimensions (in mm) of the calorimeter barrel and forward endcap.

The calorimeter is expected to achieve a mass resolution for π^0's of 4.5 to 8.3 MeV/c^2.

Since CsI crystals were chosen for the electromagnetic calorimeter, ensuring the necessary high resolution and efficiency, the primary concerns are minimizing the cost and the amount of material in front of the calorimeter. In the interest of cost, the size of all internal components has been restricted and there is no backward endcap. Material between the IP and the calorimeter has been minimized in all internal components. The largest contributor to radiation lengths in front of the calorimeter is the DIRC ($T \sim 0.18$ X_0). The total amount of material including the beampipe, vertex tracker, drift chamber and DIRC represents $T \sim 0.23$ X_0 at normal incidence. The major source of material in front of the endcap is the drift chamber endplate ($T \sim 0.14$ X_0) [12].

2.3.5 Instrumented Flux Return Magnet

The excellent momentum resolution necessary for the physics studies proposed at *BaBar* requires that the detector operate in a 1.5 T magnetic field. For this purpose, a large solenoidal magnet is located immediately outside of the electromagnetic calorimeter. Since approximately 18% of all B decays contain at least one muon, an instrumented flux return (IFR) muon detector has been designed to make use of the large iron structure needed for the magnet return yoke [12]. The goal is to achieve the highest muon tagging efficiency that is practically possible. Additionally, the IFR constitutes a neutral hadron calorimeter.

The IFR design consists of active detectors "sandwiched" between iron plates. Since access to the detectors will be difficult or impossible after construction, the choice of simple, reliable and low-cost detectors was imperative. The active detectors in the IFR are Resistive Plate Counters (RPCs) [12]. RPCs consist of a gas gap at atmospheric pressure enclosed between two 2 mm thick phenolic polymer (Bakelite) resistive plates. The plates are coated on their outer surfaces with graphite layers, with one plate connected to an 8 kV high voltage and the other to ground. As in the drift chamber, a charged particle traversing the gas gap produces ions. In the RPC's however, the result is a quenched spark that produces signals on external pick-up electrodes which provide x and y information. Neutral hadrons are detected by observing the characteristic length of the hadron showers (primarily π^0's and $\pi^\pm$) produced in the IFR. The selection of a gas mixture for the RPC's has not yet been made. Figure 2.17 shows a three dimensional view of the IFR component of the detector. Figure 2.18 shows a schematic of an RPC component.

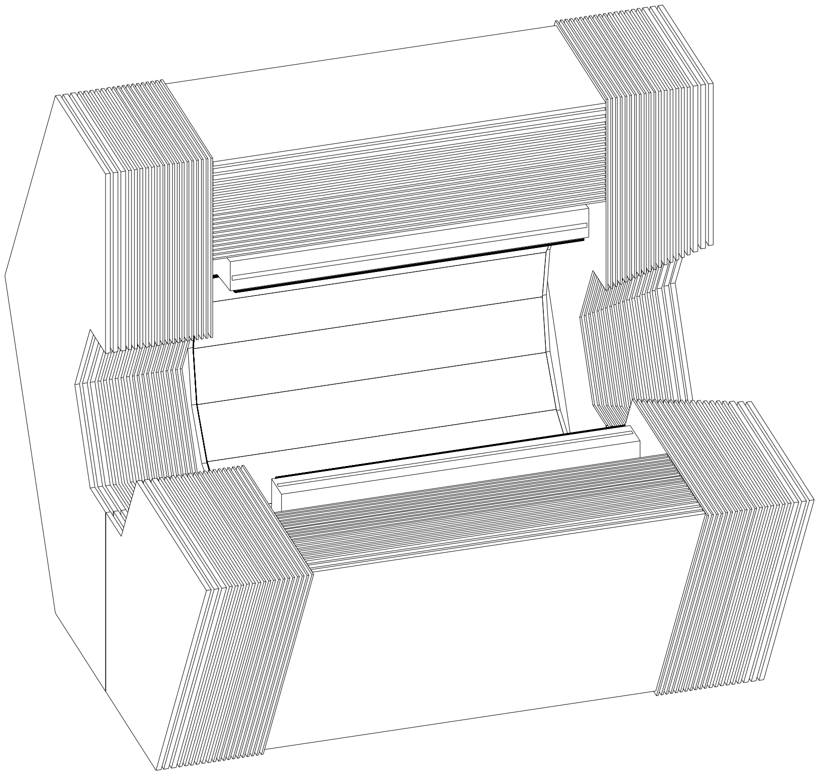

Figure 2.17: The Instrumented Flux Return detector.

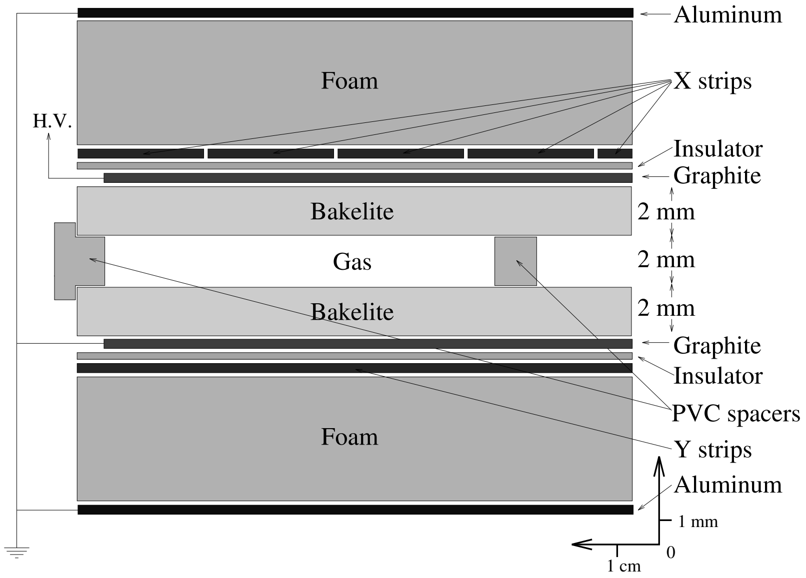

Figure 2.18: Schematic representation of the Resistive Plate Chamber components.

Chapter 3

Detector and Background Radiation Simulation

3.1 Background Radiation

As described in Sections 2.1 and 2.2, the B-Factory will produce $\Upsilon(4S)$ particles by colliding beams of electrons, e^-, and positrons, e^+, at energies of 9 GeV and 3.1 GeV respectively. The e^+/e^- are accelerated in the SLAC two-mile linear accelerator using klystrons and injected into the PEP-II storage rings where they are guided and focused by magnets for collision.

In PEP-II and *BaBar*, the main sources of background radiation are *synchrotron radiation* and *residual gas collisions* in the beampipe. These can result in photons or beam particles striking the beampipe, magnets, masks and other components in the IR producing *electromagnetic showers*. The particles produced in these showers can enter the detector where they are observed as background noise. If backgrounds are sufficiently high they can obscure the "real" signal and also cause radiation damage.

3.1.1 Synchrotron Radiation

Electrons and positrons radiate as they are accelerated and guided around bends in the accelerator. The resulting photons are referred to as synchrotron radiation. The energy of photons emitted in this process is distributed from near zero up to the energy of the primary particle, peaked at low energies and falling off rapidly to zero at the primary energy [3].

Since the storage rings necessarily pass through the detector region, the flux of synchrotron photons produced as the beams traverse the magnets is usually a primary concern in studies of background radiation.

3.1.2 Residual Gas Collisions

Further production of background radiation occurs as a result of the interaction of the particles in the beam with residual gas molecules in the beampipe. While the beam line is maintained in a very high vacuum condition, residual molecules remain in the path of the accelerated beams. Beam particles interact with molecules in the beampipe either via *Coulomb scattering* or *bremsstrahlung*. Particles which undergo either of these interactions and strike an aperture or the beam pipe are referred to as *lost beam particles*.

Coulomb Scattering

Coulomb scattering is the completely elastic scattering of a particle by the heavy nucleus of an atom. In this case, a beam particle is scattered by the nucleus of an atom in a residual molecule in the beampipe. There is no resulting change in energy of the beam particle, and therefore no resulting emitted photon. However, the path of the beam particle can change dramatically, making it incident on material in the IR.

Bremsstrahlung

Bremsstrahlung, or "braking radiation," takes the form of photons emitted as the e^+/e^- are severely accelerated by the Coulomb field of a nucleus. At high energies, the bremsstrahlung process dominates over Coulomb scattering. Like the synchrotron energy distribution, the bremsstrahlung energy distribution ranges from low energies up to the energy of the primary. However, this distribution is much flatter than that of synchrotron radiation with the probability of producing a photon of a given energy falling off as the inverse of that energy [13]. Bremsstrahlung interactions change the energy of the primary particle, often significantly. In PEP-II, this results in "off-energy" beam particles that can be swept out by the magnets in the IR, thus impinging on material in the beampipe, masks, and other components causing electromagnetic showers.

3.1.3 Electromagnetic Showers

The photons and lost beam particles arising from synchrotron radiation and bremsstrahlung can impinge on the material in the IR and the detector itself.

In the case of photons, there are three photo-processes that take place that depend on the energy of the photon involved. At high energies *pair-production* is the dominant process. This is the materialization of the photon into an e^+/e^- pair in the high field region of a nucleus. At low energies *Compton scattering* (or photon-electron scattering) is more prevalent. In the lab frame, this is the absorption of the incident photon by a free electron and consequent re-emission of a photon at a different energy. A third photo-process is the *photoelectric effect*. Here, photons impinging on matter are absorbed by bound electrons which are then emitted with some kinetic energy [1].

All of these processes result in e^+/e^- and photons which can then in turn interact with the material in the detector via bremsstrahlung, Coulomb scattering and photo-processes which in turn produce more photons and e^+/e^- which can interact via these processes and so on. The resulting multiple interaction is called an *electromagnetic cascade shower*. It should be noted that the net effect of these showers is an increase in the number of particles and a decrease in their average energy in the forward direction with each iteration of the shower process. Hence, a photon or beam particle striking some material in the IR can result in a large number of low-energy particles in the detector, deadening readout channels and causing radiation damage (also called *aging*).

The electromagnetic shower process ends when the average energy of the particles drops below the *critical energy* where ionization is the dominant process.

3.1.4 Other Background Sources

There remain other sources of background radiation that will not be discussed in this thesis. These include: e^+e^- (Bhabha) scattering, e^-e^- (Møller) scattering and cosmic rays. All of these sources are small compared to those discussed above.

3.2 Detector and Background Simulation

The PEP-II machine and all of the components of the *BaBar* detector have been simulated for the purpose of design and optimization, development and testing of the reconstruction and analysis software and, eventually, interpretation of the experimental data. Simulation is carried out using several Monte Carlo packages, each of which allows the machine and detector components to be defined by their geometries and materials. The Monte Carlo packages propagate particles through defined volumes by the generation of random numbers combined with the known behavior of the particles in the components' materials. The simulation packages used differ in the detail of their implementation, but all use random sampling of *cross-sections* (interaction probability distributions for a specific particle and process in a given material). The tools used specifically for this study of background radiation distribution in the *BaBar* drift chamber are discussed here in varying degrees of detail.

3.2.1 Tools

The steps taken in simulating background radiation in the drift chamber for this thesis were: first producing rays for input (Decay TURTLE [14]), and then tracking charged particles and photons through the detector (OBJEGS [15], GEANT [16]). Both of the latter Monte Carlo packages use similar methods for transporting particles through matter, but they differ in their capability to represent the complicated geometry of the detector and interaction region. For this reason, the more sophisticated GEANT simulation is discussed in greater detail.

3.2.2 Decay TURTLE

Decay TURTLE simulates the geometry of the PEP-II machine from the middle of the preceding arc to several meters downstream of the IP and includes all of the magnets, collimators and machine elements that will be present in the final machine. Each primary beam particle is tracked through these elements. A scattering point is chosen randomly along the beam line depending on the probability for an interaction to occur and a beam particle is transported to that point. The scattered secondary particle is then propagated along the beam line until it hits an aperture (magnet, mask or other element) or the end of the beam line (as defined by the geometry represented in Decay TURTLE). In the case of bremsstrahlung, the emitted photon is propagated as well. Particles striking an aperture near the IP are written to disk as rays for input into an OBJEGS or GEANT simulation of the detector. It should be noted that Decay TURTLE does not simulate particle interactions with matter in the detector, but rather particle motions through the magnetic fields and apertures of the storage rings near the IR. The version of Decay TURTLE used in this study has been modified to also simulate bremsstrahlung and Coulomb scattering in the beamline [14].

3.2.3 GEANT

GEANT is a Monte Carlo simulation package developed and maintained at CERN specifically for high energy physics implementation. The primary tool for simulation of the

BaBar detector is a GEANT front-end interface called BBSIM. The following sections discuss the *BaBar* implementation, but are by no means a complete discussion of GEANT's capabilities. The GEANT manual provides a detailed description of the package [16].

Method of Computing the Occurrence of a Process

Simulating the processes which occur during the propagation of a particle through matter is accomplished somewhat differently for the various Monte Carlo packages. The GEANT method, however, provides a good general description of how these packages work and a brief outline of the principles of Monte Carlo simulation is presented here [16].

First, a new particle to be tracked is fetched. In the BBSIM implementation, the new particles are rays generated by Decay TURTLE. Once the particle is fetched the number of *interaction lengths* that the particle will travel before interacting via one of the processes available is sampled. Next, the distances that the particle may travel in the current medium before any of the processes occurs is calculated. The smallest of these distances is the step over which the particle will be transported. The particle is then transported either in a straight line (in the absence of a magnetic field or in the case of a neutral particle) or along a helical path (for charged particles in a magnetic field). The energy loss of the particle is then calculated using the Bethe-Bloch formula [3]:

$$-\frac{dE}{dx} = 4\pi N_{Av} r_e^2 m_e c^2 z^2 \frac{Z}{A}\frac{1}{\beta^2}\left[ln\left(\frac{2m_e c^2\gamma^2\beta^2}{I}\right) - \beta^2 - \frac{\delta}{2}\right] \tag{3.42}$$

for a particle with charge ze passing through an element with atomic number Z and atomic weight A. The mass and classical radius of an electron are m_e and r_e, respectively, N_{Av} is Avogadro's number, and c is the speed of light. The value $I \approx 16Z^{0.9}$eV for $Z > 1$ and is referred to as the ionization constant. The γ is the relavistic boost of the particle, and $\beta = v/c$, where v is the velocity. Finally, the shielding of the nucleus by the charge density of atomic electrons is accounted for by δ which approaches $2ln\gamma$ plus a constant for very energetic particles [3].

Once the energy loss is calculated, and if a physical discrete process has occurred, the final state of the interaction is generated. In the case where the incident particle survives the interaction (for example, in bremsstrahlung) the number of interaction lengths for the surviving particle is calculated. These steps are repeated until the particle either leaves the detector or disappears in an interaction.

The interaction length, or mean free path, λ, for a particle to interact via a specific process in a medium is the inverse of its macroscopic cross-section for that process, Σ, in that medium. The macroscopic cross-section is given by:

$$\Sigma = N_{Av}\rho \sum_i \frac{p_i}{A_i}\sigma(E, Z_i, A_i) \tag{3.43}$$

where N_{Av} is Avogadro's number, Z_i is the atomic number of the i^{th} element, A_i is atomic weight, ρ is density, σ is the total microscopic cross-section for the reaction, p_i is the proportion by weight of the i^{th} element in the material and E is the energy of the particle [16].

The method for defining detector volumes and for simulating specific physical processes is discussed in the following sections.

Detector Volumes

In GEANT, component volumes are defined by a shape identifier, shape parameters and physical properties. Volumes can be placed within other volumes and positioned by the definition of a reference frame. In the BBSIM simulation, the z-axis is defined as along the direction of the high energy (electron) beam.

Since GEANT provides a wide variety of shape identifiers, the BBSIM package is able to provide a detailed simulation of the beam line components in the IR. Specifically, BBSIM includes an approximation to the complex geometry of the synchrotron radiation masks, which have elliptical apertures. Also included in the IR simulation are the B1 and Q1 beam line magnets with their dipole and quadrupole fields as well as the Q2 septum masks that shield the Q2 coil. Figure 3.19 shows the IR region of the simulation and a sample event. An incoming positron (LEB particle) scatters off of a synchrotron radiation mask tip producing a shower of electrons, positrons and photons.

For the purpose of studying the background distribution in the drift chamber, all interior volumes are simulated. In addition to the IR, the silicon vertex detector and the support tube are included in the simulation, as they are between the IP and the drift chamber.

The drift chamber is defined as a cylinder with an inner radius 22.5 cm and an outer radius 82 cm with 22.7° angled aluminum endplates, and carbon fiber inner and outer cylindrical tubes. It is offset from the interaction point such that its length is 1.1 m in the backward direction and 1.7 m in the forward direction. In BBSIM the material in the drift chamber is modeled as a Helium:isobutane mixture (80:20) with the aluminum field wires and tungsten sense wires treated as vapors and added to the mix. The result is a homogeneous mixture of gas and wires. This approximation is adequate for the purposes of background simulations since no detector readout is modeled.

The only exterior factor pertaining to the study of backgrounds in the drift chamber is the 1.5 T external magnetic field. A field map of the magnetic field is included in the BBSIM simulation.

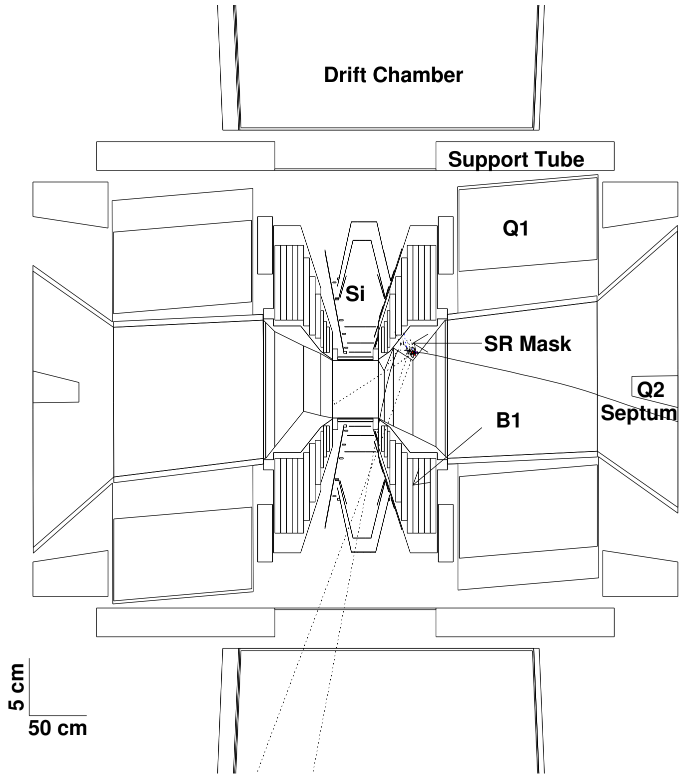

Figure 3.19: GEANT simulation of beam line (IR) components. The interaction of a LEB lost beam particle is also shown. The solid line is the incoming positron and the dotted lines are produced photons.

Monte Carlo Technique

Monte Carlo techniques are used to simulate random behavior on a computer. A common method of Monte Carlo simulation, and the one used in GEANT, is the composition and rejection method [3, 16, 17].

This method requires that the probability density function, $f(x)$, for a process is well enough known that it can be computed for any x and its shape enclosed entirely within a shape which is C times a simple distribution $h(x)$. Often $h(x)$ is a uniform distribution or a sum of uniform distributions. Both $f(x)$ and $h(x)$ are normalized, meaning that $C > 1$.

A candidate x is generated by a random number generator according to $h(x)$. The values of $f(x)$ and $Ch(x)$ are calculated. Next, another random number, u, is generated on the interval (0,1). If $uCh(x) \leq f(x)$, x is accepted. Otherwise, the process is repeated until a suitable x is found. If x and $uCh(x)$ are considered to combine as points on a two-dimensional plot, these points fill the area of $Ch(x)$ in a smooth manner and points under $f(x)$ are accepted.

The efficiency of this method is simply the ratio of areas, or $1/C$. It is therefore desirable that C be kept close to 1.0. Accordingly, $Ch(x)$ is chosen to be as close to $f(x)$ as possible using sums of uniform distributions. This is known as importance sampling, since more trial values of x are generated in the peak regions of $f(x)$ [3].

Synchrotron Radiation

A study was done prior to the research presented in this thesis optimizing the placement of the water-cooled synchrotron radiation masks inside the B1 magnet. Synchrotron radiation will be effectively minimized in the *BaBar* detector. Detailed treatment of the simulation, design and optimization of the masks can be found in [18, 20]. These studies show that in the *BaBar* detector, synchrotron radiation is a very small effect when compared to lost beam particle backgrounds. Consequently, synchrotron radiation has not been included in the studies discussed in this thesis.

Residual Gas Collisions

With the minimization of synchrotron radiation, the largest contributor to backgrounds in the *BaBar* drift chamber becomes the interaction of the beam particles with residual molecules in the beampipe. These interactions can result in high-energy beam particles and photons striking masks and the beampipe near the IP and producing electromagnetic showers.

In a bremsstrahlung interaction, the primary particle is not stopped but continues at a different energy and a photon is produced. Hence, both the scattered particle and a photon must be tracked in a simulation after the interaction. The total cross-section, σ_B for bremsstrahlung is given by [3]:

$$\sigma_B \sim \frac{\alpha^3 Z^2}{m_e^2 c^4} \tag{3.44}$$

where $\alpha \equiv e^2/\hbar c$, Z is the atomic number of the nucleus and m_e is the mass of the electron/positron.

Energy loss for a beam particle due to bremsstrahlung is given by [3]:

$$\frac{dE}{dx} = -\frac{E}{X_0} \tag{3.45}$$

where E is the initial particle energy, x is the distance traveled in the medium and X_0 is the radiation length of the particle in the medium. The radiation length for electron/positron bremsstrahlung is defined as [3]:

$$\frac{1}{X_0} = \frac{4Z(Z+1)r_e^2 N_{Av}}{137A} ln\left(\frac{183}{Z^{1/3}}\right) \tag{3.46}$$

where r_e is the classical electron radius and A is the mass number of the nucleus.

The bremsstrahlung photon is then propagated through the medium as is the electron/positron at its lower energy. Either of these can then interact again.

Electromagnetic Showers

In the case of the photoelectric effect, the incident photon is stopped and the energy of the "knock off" electron is calculated and the electron propagated. The macroscopic cross-section, Σ, for the photoelectric effect is calculated as:

$$\Sigma = \rho\sigma \tag{3.47}$$

where ρ is the medium density and σ is the microscopic cross-section [16]. For this simulation, fits were performed in different intervals j of the photon energy and for such an interval, the microscopic cross-section is given by [16]:

$$\sigma_{ij} = \frac{C_{1,ij}}{E_\gamma} + \frac{C_{2,ij}}{E_\gamma^2} + \frac{C_{3,ij}}{E_\gamma^3} + \frac{C_{4,ij}}{E_\gamma^4}(cm^2 g^{-1}) \tag{3.48}$$

with j changing from 1 to m_i, where m_i is the number of fitting intervals used for the element i. For composites or mixtures of N elements, the cross-section for the j^{th} element is calculated as:

$$\sigma_j = \sum_{k=1}^{N} f_k \sigma_{j,k} \tag{3.49}$$

where f_k is the fraction by mass of the k^{th} element in the material. Therefore:

$$C_{i,total} = \sum_{k=1}^{N} f_k C_{i,jk} \tag{3.50}$$

for $i = 1$ to 4 [16].

For Compton scattering, the quantum mechanical Klein-Nishima differential cross-section is randomly sampled to determine the energy of the scattered photon. The differential cross-section is given by [16]:

$$\Phi(E, E') = \frac{X_0 n \pi r_e^2 m_e}{E^2} \left[\frac{1}{\epsilon} + \epsilon\right] \left[1 - \frac{\epsilon \sin\theta^2}{1 + \epsilon^2}\right] \tag{3.51}$$

where E is the energy of the incident photon, E' is the energy of the scattered photon, ϵ is E'/E, n is the electron number density of the material, r_e is the classical electron radius, m_e is the mass of the electron and X_0 is the radiation length of a photon in the material.

Assuming an elastic collision, the scattering angle, θ, of the scattered photon is given by the Compton formula [16]:

$$\theta = \cos^{-1}\left[1 - \frac{m_e}{EE'}(E - E')\right] \tag{3.52}$$

For pair production, the incident photon is again absorbed and the e^+/e^-pair is tracked and can interact. The total cross-section of e^+/e^- pair production by a photon is parameterized as [16]:

$$\sigma(Z, E_\gamma) = A(Z + 1)(F_1(X) + F_2(X)Z + F_3(X)/Z) \tag{3.53}$$

in barn/atom, where $X = ln(E_\gamma/m_e)$, m_e = electron mass, E_γ = photon energy, and $F_i(X) = \sum_{n=0}^{5} c_n X^n$. The parameters c_n are taken from a least squares fit to actual data. This parameterization is applicable for a range of atomic numbers from 1 to 100 and to incident photon energies of 1.5 MeV to 100 GeV [16].

The energy of one of the particles in the e^+e^- pair is given by [16]:

$$E = \epsilon E_{\gamma} \tag{3.54}$$

where the variable ϵ is restricted kinematically to the range $m_e/E \leq \epsilon \leq 1 - m_e/E$. The cross-section is symmetric with respect to the interchange of ϵ with $1 - \epsilon$. Therefore, we can restrict ϵ to lie within the range $\epsilon_0 \leq \epsilon \leq 1/2$ where $\epsilon_0 = m_e/E$. The differential cross-section is then given by [16]:

$$\frac{d\sigma}{d\epsilon} = \sum_{i=1}^{2} \alpha_i f_i(\epsilon) g_i(\epsilon) \tag{3.55}$$

where the functions $f_i(\epsilon)$ are given by [16]:

$$f_1(\epsilon) = \frac{3}{(0.5 - \epsilon_0)^3}(\epsilon - 0.5)^2 \tag{3.56}$$

$$f_2(\epsilon) = \frac{1}{0.5 - \epsilon_0} \tag{3.57}$$

and represent conservation of energy and momentum. The functions α_i and g_i are complicated functions which account for the shielding of the nucleus by atomic electrons. A more detailed derivation of these functions is found in [16].

Output

Results from the background simulation using the BBSIM GEANT interface are output in HBOOK [21] files. HBOOK allows for the storage of one and two dimensional histograms and ntuples. In this application the x, y, z, r, and ϕ of a drift chamber hit, the radius of curvature of the tracked particle at each step, the energy loss of the particle, the layer number of the hit, and the track number of the particle producing the hit are stored in a one dimensional HBOOK ntuple.

The HBOOK file is then read into PAW [23], an interactive utility for visualizing experimental data for analysis. PAW was developed and is maintained at CERN and is a very powerful tool for high energy physics analysis.

3.2.4 OBJEGS

The first Monte Carlo simulation package used to simulate the *BaBar* drift chamber was OBJEGS. This package is an interface to EGS4 (Electron Gamma Simulation 4) [22], a widely used Monte Carlo. OBJEGS was designed to facilitate the input of simple detector geometries. Beam line and detector components are input in terms of the inner and outer radius, length, and material type. Rays generated by Decay TURTLE are then input one particle at a time and propagated through detector components. Finally, events are summed over time.

The OBJEGS package was not satisfactory for simulating the *BaBar* detector due to its restriction to cylindrical geometries. This restriction precluded realistic modeling of some of the more complicated components in the interaction region and the detectors. For example, the synchrotron radiation mask is not cylindrically symmetric but rather is elliptical in shape. An approximation to this shape was attempted by using two different versions of OBJEGS geometries, one for the HEB and one for the LEB. A particular geometry is then used depending on which side of the detector a particle struck. For example, a particle striking the forward end of the IR would use the LEB geometry to simulate the shower produced by that particle. For this reason, the OBJEGS simulation was used only for preliminary results on background distributions and will not be discussed here in detail. It is important to note, however, that GEANT provides a detector/geometry interface to EGS4 as well as a number of other simulation packages (GHEISHA, HADINT, EGS, to name a few). Accordingly, the previous sections on particle propagation are applicable to the OBJEGS method.

Chapter 4

Discussion of Results

This thesis discusses the results of two distinct Monte Carlo studies of the distribution of background radiation in the *BaBar* drift chamber. The first was an OBJEGS study to locate "hot spots" in the chamber volume to determine whether major design changes were necessary to exclude these high background regions. The second was a BBSIM/GEANT study of occupancies and aging carried out with a more realistic geometry simulation.

The drift chamber is still in the design stage and consequently many of the detector design parameters changed from the time of the first study to the second. In fact, the design parameters at the time of writing are different than those used in the second study. For this reason, the two simulations will be discussed separately. Also, a brief summary of the design and Monte Carlo input parameters is included in Table 4.2.

It is important to note that the changes to the design have a very minimal impact from the point of view of backgrounds in the drift chamber. The same cannot be said for other detector components. For example, the changing endplate thickness has a large effect on background rates in the forward endcap of the electromagnetic calorimeter.

4.1 Endplate Design Studies with the OBJEGS Simulation Package

The first study of background distribution in the drift chamber was carried out to determine whether radical design changes would be necessary to exclude "hot spots" from the drift chamber volume. Due to the location of the support tube immediately inside the

Table 4.2: Design and Monte Carlo input parameters for the two studies discussed as well as the current values.

	OBJEGS	BBSIM	Current
Gas mixture	He:CO_2:isobutane (78:15:7) with Al wires	He:isobutane (80:20) with Al and W wires	Same as BBSIM
Wires	50 μm Al	55 μm gold plated Al 20 μm gold plated W	80, 120 μm gold plated Al 20μm gold plated W
Endplates	None included	22.7° angled Al, 1.05 cm	flat Al, 2.4 cm
Inner wall	.5 mm Be	1.99 mm carbon fiber	1 mm Be
Outer wall	5 mm Be	3.61 mm carbon fiber	3.2 mm carbon fiber

inner radius and the offset of since the chamber in the forward direction, high occupancies were anticipated in the forward end at the inner layers (due to photon conversions in the support tube).

Several endplate designs were considered to address concerns about high backgrounds. Proposed options included highly conical endplates following the 300 mr acceptance line of the detector, as well as stepped endplates. These designs were only to be seriously considered if their benefit in terms of excluding hot spots were significant since either option would be difficult to machine and would make the wiring of the inner layers of the drift chamber problematic. These preliminary studies were undertaken using the OBJEGS interface to EGS4 discussed in Section 3.2.4.

The defined drift chamber volume was divided into 32 azimuthal segments and 28 radial layers for the purpose of background calculation. Additionally, 40 z segments were defined with a total length of 2.74 m, offset in z with 1.64 m in the $+z$ and 1.1 m in the $-z$

direction. This is the center offset of the BaBar drift chamber, chosen to optimize drift chamber performance with the boosted center of mass in the lab frame. The inner region was segmented into very thin (0.2 cm) radial "scoring layers" filled with the nominal gas mixture for better counting resolution of low momentum looping electrons in the inner layers. "Scoring layers" are small volumes defined in the larger volume of the drift chamber used purely for binning purposes. Hits in these inner layers were later averaged to reflect the actual geometry of the innermost layer of the chamber. The outer "scoring layers" were defined to approximate superlayers (see Section 2.3.2).

The gas used in the simulation was He(78%):CO_2(15%):Isobutane(7%). A multiplication factor of 0.312 was uniformly applied to the density of the helium gas mixture to approximate the presence of aluminum wires. The large number of wires in the drift chamber ($\sim$ 28000) makes including individual wires in the Monte Carlo complicated and costly. Instead, the equivalent mass and density of the wires is included evenly distributed throughout the drift chamber volume. This approximation is adequate for the purpose of studying background distribution, but is would not be satisfactory for other applications (ie. modeling chamber tracking).

Particles are tracked until their energy falls below user defined minimum energy thresholds. These energies were defined to be 0.1 MeV/c for photons and 0.611 MeV/c for electrons. Particles with energies lower than these thresholds do not contribute significantly to background rates [11].

Background rates were examined for an integration time of 4 μsec, the nominal resolving time of the OBJEGS simulated drift chamber design (PEP-II running at nominal luminosity) [11]. The OBJEGS input file specifying the geometry and cuts is included in Appendix A.

A total of 1502 events were simulated with an initial input of 10000 rays generated by Decay TURTLE, representing a total of 789 μs of beam. While background events are relatively rare, the Decay TURTLE rays used as input were saved specifically for background analysis purposes, ie. they involved the beam particle or photon striking the beam pipe, a synchrotron mask or other aperture near the IP. Since all input rays are preselected to be likely background producing candidates, the input of 10000 rays resulted in events approximately 10% of the time, much higher than normal rates. This was done purely to save computing time. Results are all calculated using the full beam time simulated (789 μs) and are therefore absolute background rates in real time. In other words, 789 μs of simulated beam time resulted in 10000 potentially interesting events that were then put in to the Monte Carlo. The bunch crossing rate is 238 MHz (4.3 ns bunch separation) so that the 789 μs of simulation represents $\approx 1.8 \times 10^5$ bunch crossings.

Backgrounds from both the HEB and LEB interacting with synchrotron radiation masks both upstream and downstream were studied. Since the goal was to look at background distributions along the chamber length (z) in order to address the endplate design issues, no ϕ distinction was made in the preliminary analysis.

Figures 4.20 and 4.21 show the results of this study. Here, HEB$^-$ refers to the high energy beam incident on the upstream (low energy beam entrance) mask, HEB$^+$ the HEB incident on the downstream mask, and so on. Photon rates are not insignificant, peaking as high as 45 per 4 μsec in the +0.125 to +0.375 m region of the detector for the HEB$^+$. Note that while the peaks are indeed shifted in the z direction, these shifts are all contained within $\pm$0.5 m and therefore the use of the proposed highly conical or stepped endplates would not eliminate the peak regions.

The relative intensity of background electron radiation is 3 orders of magnitude smaller than that of the photons. The z-distributions, shown in Figure 4.21, were found to be more uniform in all but the innermost layer of the detector. However, rates remain the most intense within the region of $\cos\theta < 300$ mrad. The relatively low occupancies, which peak at less than 1 electron per 4 μsec, suggest that the slight improvements afforded by the proposed endplates would not be worth the design difficulties.

The conclusion of the endplate design study is that there is no advantage to radically altering the flat endplate design for the purpose of excluding areas of high occupancy in the inner layers of the drift chamber.

4.2 Occupancy Studies

Chamber occupancy is defined as the fraction of cells that contain random hits during the event resolving time (nominally 1μs for the BBSIM design). If the occupancy exceeds a few percent per wire per resolving time, pattern recognition for tracking becomes impossible. Simulations to determine occupancy were carried out using the GEANT interface BBSIM discussed in Section 3.2.3.

The chamber geometry defined for the BBSIM simulation is very similar to that in the previous section. The chamber length is 2.8 m with an inner radius of 22.5 cm and an outer radius of 80 cm. The volume is filled with a He(80%):Isobutane(20%) mixture with aluminum and gold plated tungsten wires modeled as vapors. The resolving time is defined as the maximal drift time of the chamber and is set to 1 μsec as determined in studies of cell geometries and gas mixtures [12]. All components between the drift chamber and the IP are included in the model including the silicon vertex detector, the beryllium support tube, and the beam pipe. Additionally, the IR components within the fiducial volume of the drift chamber are modeled, including the synchrotron radiation masks. A very good approximation to the actual shape of the masks is possible due to the greater flexibility of the BBSIM interface to GEANT. The input geometry used for this simulation is included in Appendix B.

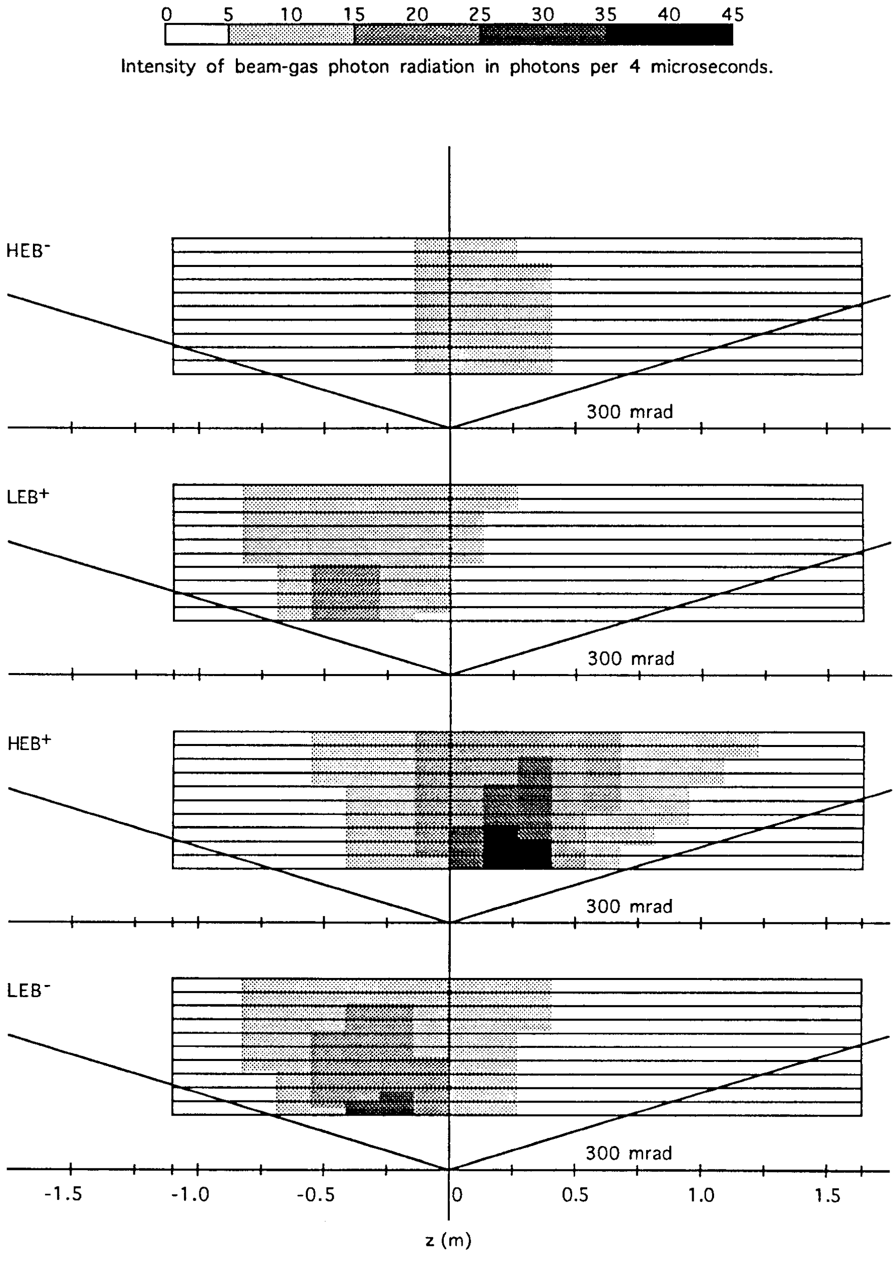

Figure 4.20: z distribution intensity of beam-gas photon radiation in photons/4 μsec. The label HEB^- means the high-energy beam incident on upstream mask, LEB^+ the low-energy beam on the downstream mask, and so on.

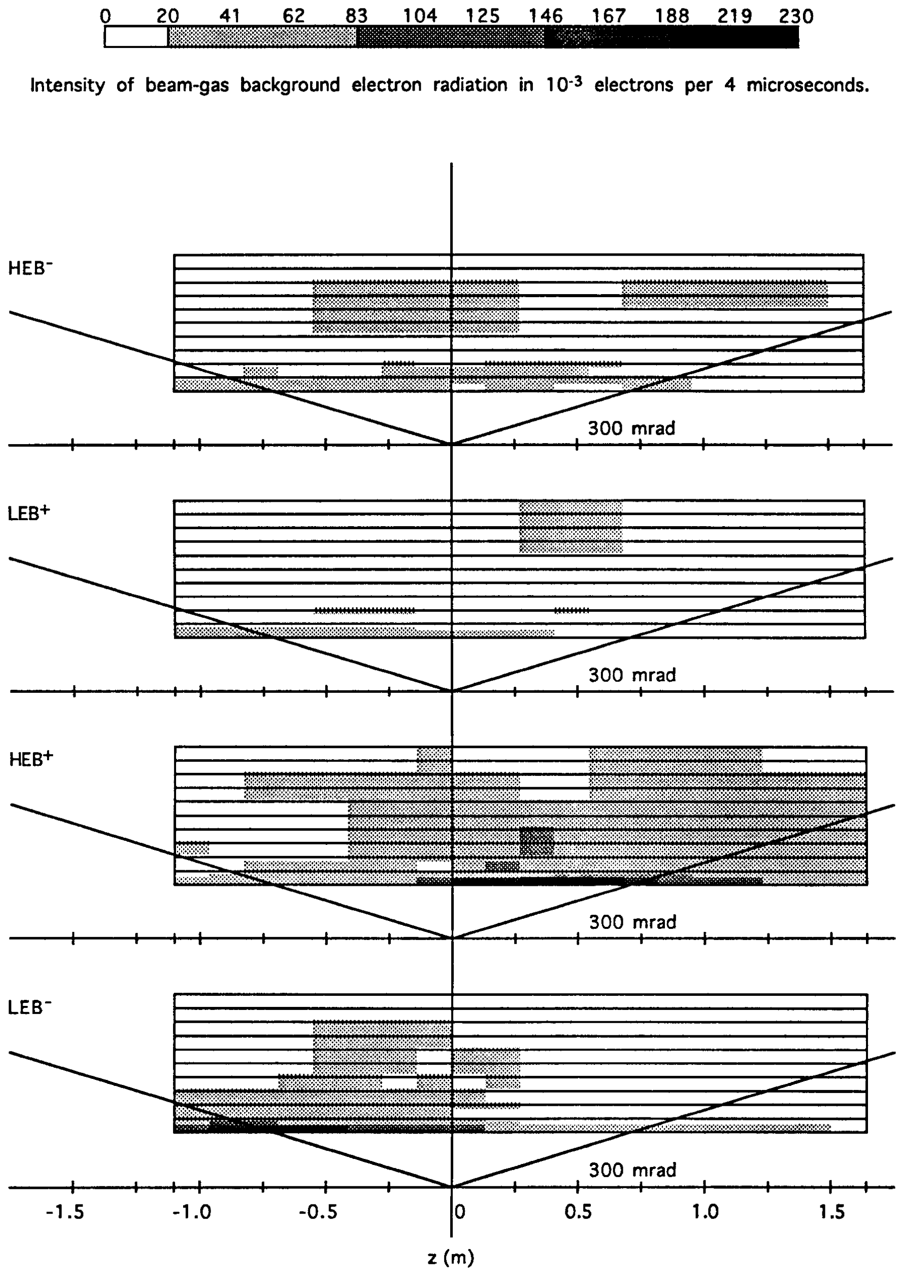

Figure 4.21: z distribution intensity of beam-gas electron radiation in 10^{-3} electrons/4 μsec. The label HEB^- means the high-energy beam incident on upstream mask, LEB^+ the low-energy beam on the downstream mask, and so on.

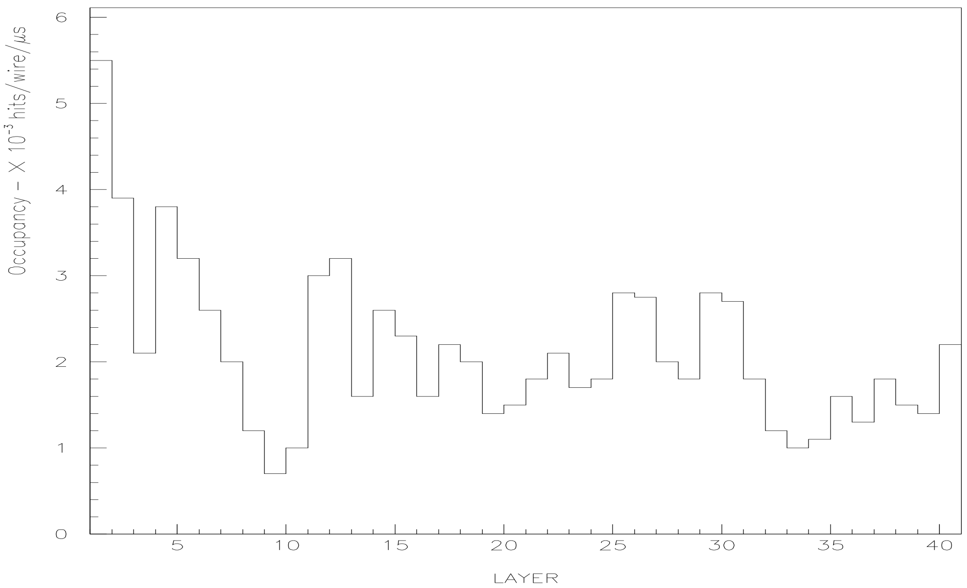

Figure 4.22: Simulated background occupancies for each drift chamber layer due to converted photons from showers produced by lost particle interactions.

A total of 10000 Decay TURTLE rays were input representing 789.9 μs. As mentioned in the previous section, the results are calculated using the full beam time of 789.9 μs. The results for the occupancy simulations are shown in Figure 4.22.

The occupancy distribution is peaked at the innermost layers with expected occupancies of 0.55% wire^{-1} μs^{-1}. This peak is expected due to photon to e^+/e^- conversions in the support tube immediately outside of the drift chamber inner wall. The average occupancy in the outer layers is 0.16% wire^{-1} μs^{-1}. The smearing of the occupancies in the outer layers is due to the modeling of the wires as vapors, the actual occupancies are expected to be significantly lower in the outer layers. Pattern recognition becomes very difficult when occupancies reach the level of ~10%. These occupancies are then well within acceptable levels according to this simulation. It should be noted, however, that no attempt has been made to address the impact of cross-talk (pulses produced in

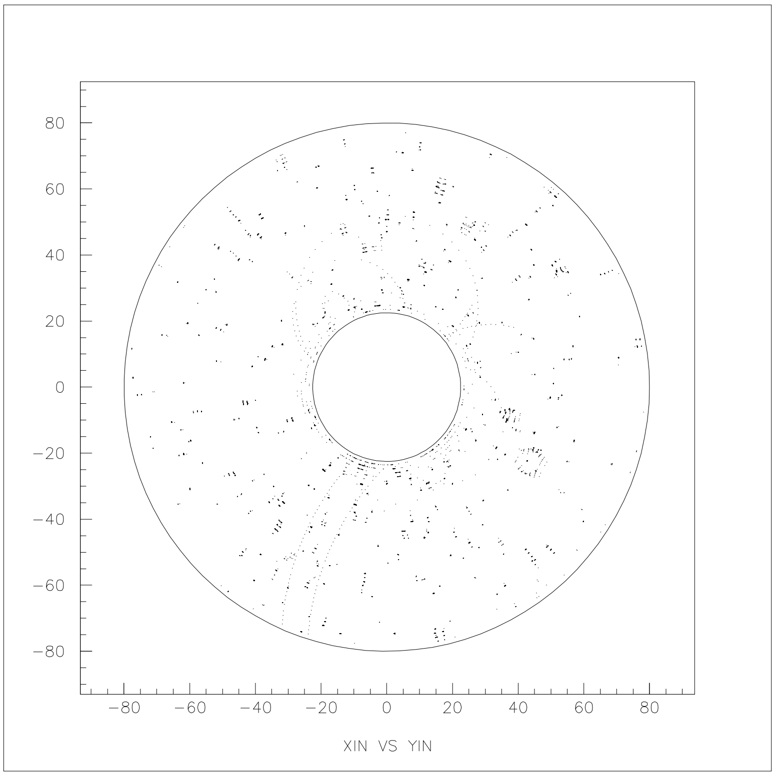

Figure 4.23: The background distribution in ϕ.

neighboring wires due to a large pulse on a given wire). Since background events will tend to produce low momentum particles that will loop tightly in the inner layers, depositing large amounts of charge on a few wires, the effect of cross-talk might be large.

Figure 4.23 shows the ϕ distribution of background events integrated over 789.9 μs. Once again higher rates are observed at the innermost layers.

Figure 4.24 shows the energy deposited per layer for all events. This distribution is noticeably peaked below 5 MeV/c.

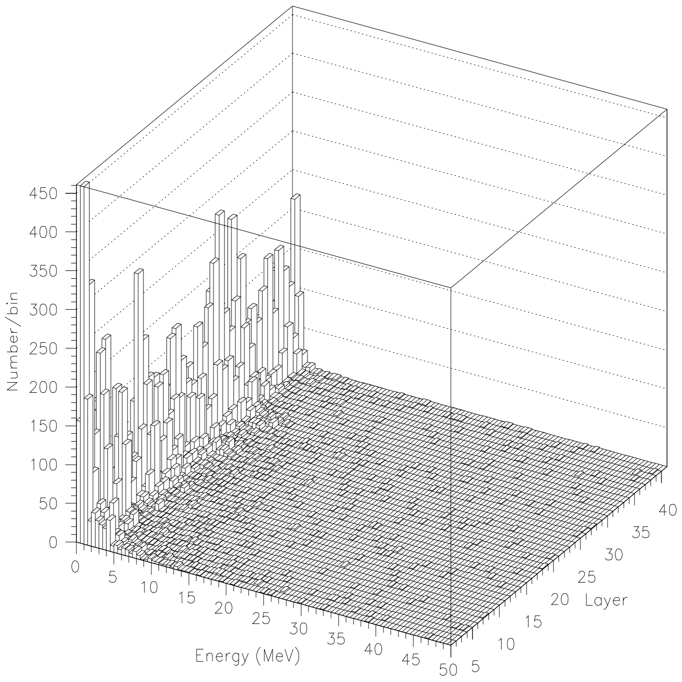

Figure 4.24: Energy distribution per layer in MeV for integration time of 789.9 μs. All energy deposits greater than 50 keV are shown as entries in the histogram.

4.3 Aging Studies

Aging in the drift chamber is defined as changes in gain or increases in noise due to material deposited on the wires from the gas-avalanche process. Using the BBSIM simulation described above, the charge deposition on a wire corresponds to an integrated charge of 0.001 C/cm/10^7 sec for the innermost drift chamber layer. This value is calculated as follows:

$$\text{accumulated charge} = (E/I)e/\ell \tag{4.58}$$

where E is the energy deposited in some time interval in a given layer, I is the effective ionization energy of the gas mixture, e is the charge of an electron and ℓ is the length of the wire in the layer. Values are quoted for uniform distribution along the wires. In fact, as shown in Figure 4.21, there is a factor of $\sim$2 or more variation in the distribution in z. Taking this variations into account, the expected integrated charge for some regions in the inner layers may be as high as 0.005 C/cm/10^7 sec. This significant amount of charge will lead eventually to deposits of hydrocarbons on the wires. These deposits will result in sparking and current draw. A value of 0.1 C/cm is generally considered to be a conservative limit on the tolerable integrated charge on a wire. This would give the drift chamber an expected lifetime of at least 6 years, which is acceptable.

Chapter 5

Conclusions

The simulations of the distribution of background radiation in the *BaBar* drift chamber presented in this thesis sought to address endplate shape/design issues, occupancies and drift chamber aging.

The studies showed that the background distribution was peaked at the inner layers and in the forward direction, as anticipated due to the location of the support tube immediately outside the drift chamber inner wall and due to the offset in the forward direction. However, rates are not expected to be especially problematic and radical design considerations like highly conical or stepped endplates are not considered necessary. Indeed, the difficulty in machining such endplates and in mounting electronics on the inner layers far outstrips the benefits they would afford in terms of excluding hot spots from the drift chamber volume. The final design will include a flat backward endplate and a flat forward endplate with one step.

Occupancies were shown to be well within acceptable limits with a peak in the inner layers of 0.55% wire^{-1} μs^{-1} and an average in the outer layers of 0.16% wire^{-1} μs^{-1}. If occupancies reach the level of approximately 10% wire^{-1} μs^{-1}, pattern recognition would become extremely difficult. However, cross-talk has not been accounted for in this study and might have a significant effect on the performance of the inner layers.

Aging estimates based on occupancy studies show an expected drift chamber lifetime of approximately 6 years. This is an acceptable value with a goal for major chamber refurbishing or upgrade of approximately 5 years from turn-on.

Appendix A

OBJEGS Input File

The following is an actual input file for OBJEGS Monte Carlo simulation. All geometry, materials and magnetic fields are specified.

AP75HI DATA A1

This OBJEGS runcard file defines masking and detector for the Apiary 6.3 flat-beam B-Factory lattice. See Hearty *BABAR*Note [15].

Mod 8/14/91 by Hobey DeStaebler to be very appro Apiary 7.3

1. HEB sees Q1 only; LEB both Q1,Q2
2. LEB off axis in Q1.
3. No change in detector, just beamline.
4. Magnets, offsets from Mike Sullivan
5. Change B1 7.5 kG, 45cm long, start 25 cm.
6. Q1 becomes G=1.03 Kg/cm, z=90-210 cm.
7. Estimate radii from Ap 6.3 OBJEGS
8. Slice magnets–at least 10 slices per kind of field.
9. Distinguish DEB (w=+1) and LEB (w=-1) directions.

In table below, a = medium 1 = Ta, 2 = Fe, 3 = Al, 4 = Be, 5 = Cu, 6 = Pb, 7 = CO2(92)/Ethane(8) 2 atm, 8 = W, 9 = He(78)/C02(15)/Isobutane(7), 10 = Sm2Co17, 11 = Ar(50)/ethane(50), 12 = Ar(80)/Methane(20) 8.6 atm, 13 = C226, 14 = ti, 15 = NaI, 16 = Si, 17 = CsI, 18 = LAr, 19 = G10 b and c control information recorded in IDA or handypak:

b = 0 photons or electrons, b = 1 electrons only

c = 0 neither ida nor handypak, c = 1 handypak only, c = 2 ida and handypak

d and bfield are used to define magnetic regions

name	z left	z right	r inner	r outer	a	b	c	d	bfield
% BEGOBJ									
Support 2	60.	900.	16.8	18.0	3	0	0	0	0.0
Quad 1A	90.	120.	7.0	12.	10	0	0	0	0.0
Quad 1B	120.	150.	7.0	12.0	10	0	0	0	0.0
Quad 1C	150.	180.	7.0	12.	10	0	0	0	0.0
Quad 1D	180.	210.	7.0	12.	10	0	0	0	0.0
Q1 Shield	90.	210.	12.	15.	8	0	0	0	0.0
B1	20.	25.	3.75	5.08	10	0	0	0	0.0
B1	25.	30.	4.00	6.80	10	0	0	0	0.0
B1	30.	35.	4.25	8.05	10	0	0	0	0.0
B1	35.	40.	4.5	9.40	10	0	0	0	0.0
B1	40.	45.	4.75	9.92	10	0	0	0	0.0
B1	45.	50.	5.00	10.44	10	0	0	0	0.0
B1	50.	55.	5.25	10.96	10	0	0	0	0.0
B1	55.	60.	5.5	11.48	10	0	0	0	0.0
B1	60.	65.	5.75	12.01	10	0	0	0	0.0
B1	65.	70.	6.00	12.53	10	0	0	0	0.0
BEAMPIPE 4	210.	430.	6.0	6.4	5	0	0	0	0.0
ENDCAP 0A	150.	154.	45.	50.	17	0	0	0	0.0
ENDCAP 0B	154.	160.	45.0	50.0	17	0	0	0	0.0
ENDCAP 0C	160.	187.	45.0	50.0	17	0	0	0	0.0

name	z left	z right	r inner	r outer	a	b	c	d	bfield
ENDCAP 1	150.	154.	50.0	100.0	17	0	0	0	0.0
ENDCAP 2	154.	160.	50.0	100.0	17	0	0	0	0.0
ENDCAP 3	160.	187.	50.0	100.0	17	0	0	0	0.0
EC Shield1	187.	197.	45.0	100.0	6	0	0	0	0.0
EC Shield2	180.	154.	18.0	45.0	6	0	0	0	0.0
EC Shield3	154.	197.	40.0	45.0	6	0	0	0	0.0
MASK G	70.	90.	7.0	11.0	8	0	0	0	0.0
MASK H	210.	280.	6.7	10.7	8	0	0	0	0.0
MASK I	330.	430.	6.7	10.7	8	0	0	0	0.0
Catcher	430.	450.	0.	12.	8	0	0	0	0.0
% Duplicate									
Quad 2-	-330.	-280.	6.7	13.	10	0	0	0	0.0
MASK J+	280.	330.	6.7	8.7	8	0	0	0	0.0
MASK	-86.4120	-70.0	5.0	5.2	1	0	0	0	0.0
MASK	-84.4120	-65.5	4.8	5.0	1	0	0	0	0.0
MASK	-82.4120	-61.0	4.6	4.8	1	0	0	0	0.0
MASK	-80.4120	-56.5	4.4	4.6	1	0	0	0	0.0
MASK	-78.4120	-52.6	4.2	4.4	1	0	0	0	0.0
MASK	-76.4120	-47.5	4.0	4.2	1	0	0	0	0.0
MASK	-74.4120	-43.0	3.8	4.0	1	0	0	0	0.0
MASK	-72.4120	-38.5	3.6	3.8	1	0	0	0	0.0
MASK	-70.4120	-34.0	3.4	3.6	1	0	0	0	0.0
MASK	-68.4120	-29.5	3.2	3.4	1	0	0	0	0.0
MASK	-66.4120	-25.0	3.0	3.2	1	0	0	0	0.0

name	z left	z right	r inner	r outer	a	b	c	d	bfield
MASK	-64.4200	-19.5	2.8	3.0	1	0	0	0	0.0
MASK	-62.2619	-14.5	2.6	2.8	1	0	0	0	0.0
MASK	-60.2699	-8.5	2.5	2.6	1	0	0	0	0.0
MASK	-60.2699	-8.6	2.4	2.5	1	0	0	0	0.0
MASK	-58.2779	-13.2918	2.2	2.4	1	0	0	0	0.0
MASK	-56.1199	-18.1059	1.0	2.2	1	0	0	0	0.0
MASK	-54.1279	-23.0859	1.8	2.0	1	0	0	0	0.0
MASK	-52.1359	-27.8999	1.6	1.8	1	0	0	0	0.0
MASK	-49.9779	-32.7139	1.4	1.6	1	0	0	0	0.0
MASK	-47.9859	-34.6939	1.2	1.4	1	0	0	0	0.0
MASK	-45.9939	-42.5079	1.0	1.2	4	0	0	0	0.0
BEAMPIPE 1	-8.5	+8.5	2.5	2.6	4	0	0	0	0.0
BEAMPIPE 0	-8.5	+8.5	2.4975	2.5	5	0	0	0	0.0
BEAMPIPE-3	-210.	-86.412	5.0	5.2	5	0	0	0	0.0
MASK 1	-210.	-205.	5.2	6.4	1	0	0	0	0.0
BEAMPIPE+2	8.5	11.8	2.59	2.79	5	0	0	0	0.0
BEAMPIPE+2	11.8	15.1	2.68	2.88	5	0	0	0	0.0
BEAMPIPE+2	15.1	18.4	2.77	2.97	5	0	0	0	0.0
BEAMPIPE+2	18.4	21.7	2.86	3.06	5	0	0	0	0.0
BEAMPIPE+2	21.7	25.0	2.95	3.15	5	0	0	0	0.0
BEAMPIPE+3	25.	28.	3.06	3.26	5	0	0	0	0.0
BEAMPIPE+3	28.	31.	3.17	3.37	5	0	0	0	0.0
BEAMPIPE+3	31.	34.	3.28	3.48	5	0	0	0	0.0
BEAMPIPE+3	34.	37.	3.39	3.59	5	0	0	0	0.0
BEAMPIPE+3	37.	40.	3.50	3.70	5	0	0	0	0.0

name	z left	z right	r inner	r outer	a	b	c	d	bfield
BEAMPIPE+4	40.	43.	3.65	4.05	5	0	0	0	0.0
BEAMPIPE+4	43.	46.	3.80	4.20	5	0	0	0	0.0
BEAMPIPE+4	46.	49.	3.95	4.35	5	0	0	0	0.0
BEAMPIPE+4	49.	52.	4.10	4.50	5	0	0	0	0.0
BEAMPIPE+4	52.	55.	4.25	4.65	5	0	0	0	0.0
BEAMPIPE+4	55.	58.	4.40	4.80	5	0	0	0	0.0
BEAMPIPE+4	58.	61.	4.55	4.95	5	0	0	0	0.0
BEAMPIPE+4	61.	64.	4.70	5.10	5	0	0	0	0.0
BEAMPIPE+4	64.	67.	4.85	5.25	5	0	0	0	0.0
BEAMPIPE+4	67.	70.	5.00	5.40	5	0	0	0	0.0
BEAMPIPE+4	70.	73.	5.15	5.55	5	0	0	0	0.0
BEAMPIPE+4	73.	76.	5.30	5.70	5	0	0	0	0.0
BEAMPIPE+4	76.	79.	5.45	5.85	5	0	0	0	0.0
BEAMPIPE+4	79.	82.	5.60	6.00	5	0	0	0	0.0
BEAMPIPE+4	82.	210.	6.	6.4	5	0	0	0	0.0
SUPPORT 1	-60.	60.	19.7	21.0	-13	0	0	0	0.078
SI LAY 1	-4.5	4.50	2.8	2.83	+16	0	0	0	0.0
SI LAY 2	-9.0	9.00	5.1	5.13	+16	0	0	0	0.0
SI LAY 3	-9.0	9.00	7.4	7.43	+16	0	0	0	0.0
SI LAY 4	11.0	11.03	4.0	8.5	+16	0	0	0	0.0
SI LAY 5	14.0	14.03	4.0	8.5	+16	0	0	0	0.0
DC WALL	-110.	164.	22.5	22.55	4	0	3	0	0.0
DC OTHER 1	-110.	164.	22.55	23.	-9	0	0	0	.312
Support 3	-110.	164.	23.	23.4	-13	0	0	0	0.078

name	z left	z right	r inner	r outer	a	b	c	d	bfield
DC OTHER 2	-110.	164.	23.40	24.08	-9	0	1	0	.312
DC SCORE 1	-110.	164.	24.O8	24.28	-9	0	1	0	.312
DC SCORE 2	-110.	164.	23.28	24.48	-9	0	1	0	.312
DC SCORE 3	-110.	164.	23.48	24.68	-9	0	1	0	.312
DC SCORE 4	-110.	164.	23.68	24.88	-9	0	1	0	.312
DC SCORE 5	-110.	164.	23.88	25.08	-9	0	1	0	.312
DC SCORE 6	-110.	164.	25.08	25.28	-9	0	1	0	.312
DC SCORE 7	-110.	164.	25.28	25.48	-9	0	1	0	.312
DC SCORE 8	-110.	164.	25.48	25.68	-9	0	1	0	.312
DC SCORE 9	-110.	164.	25.68	26.08	-9	0	1	0	.312
DC SCORE 10	-110.	164.	26.08	26.48	-9	0	1	0	.312
DC SCORE 11	-110.	164.	26.48	26.88	-9	0	1	0	.312
DC SCORE 12	-110.	164.	26.88	27.28	-9	0	1	0	.312
DC SCORE 13	-110.	164.	27.28	27.68	-9	0	1	0	.312
DC SCORE 14	-110.	164.	27.68	28.08	-9	0	1	0	.312
DC SCORE 15	-110.	164.	28.08	28.48	-9	0	1	0	.312
DC SCORE 16	-110.	164.	28.48	28.88	-9	0	1	0	.312
DC SCORE 17	-110.	164.	28.88	29.28	-9	0	1	0	.312
DC SCORE 18	-110.	164.	29.28	29.68	-9	0	1	0	.312
DC SCORE 19	-110.	164.	29.68	29.91	-9	0	1	0	.312
DC OTHER 3	-110.	164.	29.91	32.61	-9	0	1	0	.312
DC OTHER 4	-110.	164.	32.61	35.61	-9	0	1	0	.312
DC OTHER 5	-110.	164.	35.31	40.71	-9	0	1	0	.312
DC OTHER 6	-110.	164.	40.71	46.53	-9	0	1	0	.312

name	z left	z right	r inner	r outer	a	b	c	d	bfield
DC OTHER 7	-110.	164.	46.53	57.33	-9	0	1	0	.312
DC OTHER 8	-110.	164.	57.33	68.45	-9	0	1	0	.312
DC OTHER 9	-110.	164.	68.45	78.37	-9	0	1	0	.312
DC OUTWALL	-100.	164.	79.37	79.87	3	0	0	0	0.0
Crid	-150.	150.	80.	94.	0	0	0	0	0.0
CALOR 1	-150.	150.	94.0	98.0	17	0	0	0	0.0
CALOR 2	-150.	150.	98.0	104.	17	0	0	0	0.0
CALOR 3	-150.	150.	104.	131.	17	0	0	0	0.0
% ENDOBJ									
Det Sol	-150.	150.	0.0	94.	0	0	0	3	10.
B1+	25.	70.	0.	7.	0	0	0	2	-7.5
B1-	-70	-25	0.0	7.	0	0	0	2	7.5
Q1+	90.	210.	0.0	12.0	0	0	0	4	-1.03
Q1-	-210.	-90.	0.0	12.	0	0	0	4	-1.03
Q2-	-330.	-280.	0.0	12.	0	0	0	4	1.15
% ENDMAG									

% BEGINIT 0.600 .001 ecut and pcut

47183756402 RANDOM NUMBER SEED

100001 1 1. NCASES IQI WTHIST

% I90 E0 = 9000.0 X0 = 0.0 Y0 = 0.0 Z0 = 0.0 U0 = 0.0 V0 = 0.0 W0 = 1.0

Appendix B

BBSIM Input File

The following is the actual geometry input file for the GEANT/BBSIM runs upon which this thesis is based.

```
! History:
! 05-Nov-1995 Lockman: added origin of dhca (odcha)
! 25-Nov-1995 Rankin: modified definitions of dclay hits to use px etc.
! 10-Dec-1995 Kral: Add layer(+cell) number(s) in DCLAY+DCWIR hits for .ds.
! Remove fitter structure dcflags.
incname dcha ! include file name
!
structure dcha ! drift chamber
!
! BaBar Drift Chamber - EPAC Technical Design Report superlayer design
! From EPAC draft and the file Feb 21 17:30 /u/ec/adam/dcsim/auvw.90.18
! Updated src/dcha code to agree with dcha.db on March 16, 1995.
!
!
real rext 80. ! External radius of the drift chamber
real rref 80. ! Reference radius
real rint 22.5 ! Internal radius of the drift chamber
real dsw 0.0020 ! Sense Wire Diameter
real dfw 0.0055 ! Field Wire Diameter
```

```
! no guard wires real dgw 0.0070 ! Guard Wire Diameter
!
! Support tube: carbon fiber/rohacell foam sandwich - 0.5 % rl
! DC inner wall: 0.400 mm carbon fiber tube - 0.15 % rl
! rf shield foil: 0.130 mm aluminum - 0.15 % rl
! Equivalent to 0.8 % of X0 (carbon fiber r.l.=24.90cm)
! real ecagi 0.199 ! Cage Thickness (internal)
real ecagi 0.0747 ! Cage thickness w.out support tube (0.3%*24.9cm)
!
! Outer wall: 3.0 mm solid carbon fiber - 1.3 % rl
! rf shield foil rl 0.130 mm aluminum - 0.15 % rl
! Equivalent to 1.45% of X0 (carbon fiber)
real ecage 0.361 ! Cage Thickness (external)
!
! 6.5 mm carbon fiber end plate................ 2.8 % rl
! Sacrificial epoxy layer machined for......... 0.5 % rl
! feedthrough registration
! Feedthrough plastic longer than endplate,....
! but has longer rl - a wash to first order
! Brass wire locating feedthrough inserts...... 0.3 % rl
! aluminum crimp pins.......................... 0.3 % rl
! brass crimp pins............................ 0.3 % rl
! Equivalent to 4.2% of X0 (carbon fiber)
real ecagp 1.05 ! Cage Thickness (End-Plates)
!
```

```
!Electronics:
!(1) Backward: Preamp boards, HV, cables, etc............. 10.0 % rl
!(2) Forward: G10 boards with copper ground plane......... 0.8 % rl
! Some sort of brass connectors soldered...... 0.5 % rl
! onto the G10/copper boards.
! Forward and Backward rf shield:
! 0.5 mm aluminum sheet......................... 0.6 % rl
! Carbon fiber support spider................... 0.4 % rl
! (arbitrarily chosen to make 1% total for rf shield)
! Equivalent to 11% rl backward, 2.3% rl forward
real eelec(2) 1.03 0.22 ! Equivalent silicon thicknesses (r.l.=9.36cm)
!
! int nsl 1 ! Number of Super-Layers (10=sl, 1=no sl)
int nsl 10 ! Number of Super-Layers (10=sl, 1=no sl)
! int nlay 40 ! Number of Layers per Super-Layer(4=sl,40=no sl)
int nlay 4 ! Number of Layers per Super-Layer (4=sl, 39=no sl)
real psi(2) 22.7 22.7 ! End-Plates Psi Angles; TDR: psi(1) used for both
real zgas(2) -111.3 165.7 ! Extremal Z values (gas volume)
real z(2) -127.3 171.7 ! Extrem Z (chamb)
char dummy ”string” ! needed to avoid absurd compilation problem
! with g++ compiler
real full_length 276. ! full chamber length along z, used in auvlay.f
real cell_size 0.838666 ! (2/3)*Rectangular cell size (radially)
real max_sag 1.5 ! Max Sag for No-Super-Layer chamber (for nsl=1 only)
! 1.5 = Fixed maximum sag (cm), independent of cell height
! -1.5 = Automatically calculated = cell height
! 0.0 = All-axial no-superlayer chamber
```

```
real sigz 9999.0 ! Resolution in z (z-strips) huge!
real sigrp 0.0140 ! resolution in the drift coordinate
real zcat 0.0 ! Z-Pad Layer Thickness (0=no z-layer, 0.5=default)
real rzcat(2) 23.0 79.5
! wire phi half-angle in degrees
real dphi(10) /
0. 11.058 -10.222 0. 8.844 -8.397 0. 7.583 -7.297 0.
! Radius of first sense wire per layer, at full_length/2 "end of chamber"
real r(10) /
24.18 30.26 35.29 40.82 46.90 51.93 57.46 63.54 68.57 74.10
! Number of phi cells / superlayer
int nphi(10) 90 108 126 144 162 180 198 216 234 252
! Superlayer type (redundant with 'ster')
char tsl(10) "A" "U" "V" "A" "U" "V" "A" "U" "V" "A"
! Sense wire Layer radii at z = Z0 = waist of chamber (recalculated in code)
real rlay1(4) 99.999 99.999 99.999 99.999
real rlay2(4) 99.999 99.999 99.999 99.999
real rlay3(4) 99.999 99.999 99.999 99.999
real rlay4(4) 99.999 99.999 99.999 99.999
real rlay5(4) 99.999 99.999 99.999 99.999
real rlay6(4) 99.998 99.999 99.999 99.999
real rlay7(4) 99.999 99.999 99.999 99.999
real rlay8(4) 99.999 99.999 99.999 99.999
real rlay9(4) 99.999 99.999 99.999 99.999
real rlay10(4) 99.999 99.999 99.999 99.999
```

```
! stereo angles for each layer (recalculated in code)
real ster1(4) 0.00 0.00 0.00 0.00
real ster2(4) 0.00 0.00 0.00 0.00
real ster3(4) 0.00 0.00 0.00 0.00
real ster4(4) 0.00 0.00 0.00 0.00
real ster5(4) 0.00 0.00 0.00 0.00
real ster6(4) 0.00 0.00 0.00 0.00
real ster7(4) 0.00 0.00 0.00 0.00
real ster8(4) 0.00 0.00 0.00 0.00
real ster9(4) 0.00 0.00 0.00 0.00
real ster10(4) 0.00 0.00 0.00 0.00
! wire pattern in a superlayer
! char wpat(23) /
! ”F ” ” ” ”F S ” ” ” /
! ”F ” ” F F” ” F ” ” ” ”S F ” ” ” /
! ” F ” ” F F” ”F ” ” ” ”F S ” ” ” /
! ”F ” ” F F” ” F ” ” ” ”S F ” ” ” /
! ”F ”
! hit info
real odcha(3) 0.00 0.00 0.00 ! origin of dcha in lab
end dcha
!
!
dimension nhel_dclay 12 ! number of hit elements
index dclay /
x0 y0 z0 px0 py0 pz0 path dEdx typ time flag layer
```

```
structure dclay ! Hit structure for the layers
char set "DCHA"
char hnam(12) /
"x0" "y0" "z0" "px0" "py0" "pz0" "path" "dEdx" "typ" "time" "flag" "layer"
int hbit(12) /
32 32 32 32 32 32 32 32 16 32 32 16
real hoff(12) /
500. 500. 500. 100. 100. 100. 0. 0. 0. 1.e-5 0. 0.
real hfac(12) /
1.e4 1.e4 1.e4 1.e6 1.e6 1.e6 1.e4 1.e6 1. 1.e14 1. 1.
end dclay
!
!
dimension nhel_dcwir 9 ! number of hit elements
index dcwir x y z rcell phcell dedx drift idclay idcell
structure dcwir ! Hit structure for the sense wires
char set "DCHA"
char hnam(9) "x" "y" "z" "rcell" "phcell" "dedx" "drift" "idclay" "idcell"
int hbit(9) 32 32 32 32 32 32 32 16 16
real hoff(9) 500. 500. 500. 0. 0. 0. 500. 0. 0.
real hfac(9) 1.e4 1.e4 1.e4 1.e4 1.e5 1.e6 1.e4 1. 1.
end dcwir
!
structure dcopt ! generation/reconstruction options
int hwirtyp 1 ! 0:none, 1:one bank (default), 3:three banks
int lhwir 1 ! 0:don't store, ¿=1:store hits (default), ¿=2:hit dump
int prtdeb 1 ! debug level 0=off, 1=status (default), 2=print hits
end dcopt
```

```
template dcmat ! dcha materials template (material number assigned in dc_tmed)
int number ! material number - reassigned dynamically in dc_tmed
char name ! name
real a ! atomic weight
real z ! atomic number
real dens ! density
real radl ! radiation length
real absl ! absorption length
end dcmat
!
! He:isobutane 80:20 gas averaged with material contribution from wires
make dcmat gaz 0 "He-ibu-wire" 31. 15. .84E-03 .34E+05 .1E+06
! the following materials are not specific to the dcha. They should be defined once
make dcmat car 0 "Carbon-Fiber" 13.208 6.600 1.590 24.9 63.6
make dcmat sil 0 "Silicon" 28.090 14.000 2.330 9.36 30.3
make dcmat tug 0 "Tungsten" 183.85 74.000 19.3 0.35 10.3
!
template dcmed
int number ! medium number - reassigned dynamically in dc_tmed
char natmed ! medium name
char name ! corresponding material name
int isvol ! sensitivity
int ifield ! field flag
real fieldm ! max. field in kgauss
real tmaxfd ! max. deflection (degrees)
real stemax ! max step permitted (cm)
real deemax ! max. energy loss
real epsil ! boundary crossing precision
real stmin ! minimum step
end dcmed
```

make dcmed mot 0 "DCHA-mother" "AIR" 0 2 15. 10.0 0.5 0.02 0.01 1.0

make dcmed cag 0 "DCHA-cage" "Carbon-Fiber" 0 2 15. 10.0 0.5 0.02 0.01 1.0

make dcmed gaz 0 "DCHA-gaz" "He-ibu-wire" 1 2 15. 10.0 0.5 0.02 0.01 1.0

make dcmed fwi 0 "DCHA-fwi" "ALUMINIUM" 0 2 15. 10.0 0.5 0.02 0.01 1.0

make dcmed swi 0 "DCHA-swi" "Tungsten" 0 2 15. 10.0 0.5 0.02 0.01 1.0

!! make dcmed gwi 0 "DCHA-gwi" "ALUMINIUM" 0 2 15. 10.0 0.5 0.02 0.01 1.0

make dcmed ele 0 "DCHA-ele" "Silicon" 0 2 15. 10.0 0.5 0.02 0.01 1.0

Appendix C

BaBar Author List

LAPP Annecy, *Annecy-le-Vieux, France*

D. Boutigny, Y. Karyotakis, S. Lees-Rosier, P. Petitpas

INFN, Sezione di Bari and Università di Bari, *Bari, Italy*

C. Evangelista, A. Palano

Beijing Glass Research Institute, *Beijing, China*

G. Chen, Y.T. Wang, O. Wen

Institute of High Energy Physics, *Beijing, China*

Y.N. Guo, H.B. Lan, H.S. Mao, N.D. Qi, W.G. Yan, C.C. Zhang, W.R. Zhao, Y.S. Zhu

University of Bristol, *Bristol, UK*

N. Dyce, B. Foster, R.S. Gilmore, C.J.S. Morgado

University of Bergen, *Bergen, Norway*

G. Eigen

University of British Columbia, *Vancouver, British Columbia, Canada*

C. Goodenough, C. Hearty, J. Heise, J.A. McKenna

Brunel University, *London, UK*

T. Champion, A. Hasan, A.K. McKemey

Budker Institute of Nuclear Physics, *Novosibirsk, Russia*

A.R. Buzykaev, V.N. Golubev, V.N. Ivanchenko, S.G. Klimenko, E.A. Kravchenko,

G.M. Kolachev, A.P. Onuchin, V.S. Panin, S.I. Serednyakov, A.G. Shamov, Ya.I. Skovpen, V.I. Telnov

California Institute of Technology, *Pasadena, California, USA*

D.G. Hitlin, J. Oyang, F.C. Porter, M. Weaver, A.J. Weinstein, R. Zhu

University of California, Davis, *Davis, California, USA*

F. Rouse

University of California, IIRPA, *La Jolla, California, USA*

A.M. Eisner, M. Sullivan, W. Vernon, Y.-X. Wang

University of California, Irvine, *Irvine, California, USA*

K. Gollwitzer, A. Lankford, M. Mandelkern, G. McGrath, J. Schultz, D. Stoker, G. Zioulas

University of California, Los Angeles, *Los Angeles, California, USA*

K. Arisaka, C. Buchanan, J. Kubic, W. Slater

University of California, San Diego *La Jolla, California, USA*

V. Sharma

University of California, Santa Barbara, *Santa Barbara, California, USA*

D. Bauer, D. Caldwell, A. Lu, H. Nelson, J. Richman, D. Roberts, M. Witherell, S. Yellin

University of California, Santa Cruz, *Santa Cruz, California, USA*

J. DeWitt, D. Dorfan, A.A. Grillo, C. Heusch, R.P. Johnson, E. Kashigin, S. Kashigin, W. Kroeger, W. Lockman, K. O'Shaughnessy, H. Sadrozinski, A. Seiden, E. Spencer

Carleton University and CRPP†, *Ottawa, Ontario, Canada*

K. Edwards, D. Karlen, M. O'Neill†

University of Cincinnati, *Cincinnati, Ohio, USA*

S. Devmal, B.T. Meadows, A.K.S. Santha, M.D. Sokoloff

University of Colorado, *Boulder, Colorado, USA*

A. Barker, B. Broomer, E. Erdos, W. Ford, U. Nauenberg, H. Park, P. Rankin, J. Roy, J.G. Smith

Colorado State University, *Fort Collins, Colorado, USA*

J. Harton, R. Malchow, M. Smy, H. Staengle, W. Toki, D. Warner, R. Wilson

Technische Universität Dresden, Institut für Kern- und Teilchenphysik, *Dresden, Germany*

J. Brose, G. Dahlinger, P. Eckstein, K.R. Schubert, R. Schwierz, R. Seitz, R. Waldi

Joint Institute for Nuclear Research, *Dubna, Russia*

A. Bannikov, S. Baranov, I. Boyko, G. Chelkov, V. Dodonov, Yu. Gornushkin, M. Ignatenko, N. Khovansky, Z. Krumstein, V. Malyshev, M. Nikolenko, A. Nozdrin, Yu. Sedykh, A. Sissakian, Z. Silagadze, V. Tokmenin, Yu. Yatsunenko

University of Edinburgh, *Edinburgh, UK*

K. Peach, A. Walker

INFN, Sezione di Ferrara, *Ferrara, Italy*

L. Piemontese

Laboratori Nazionali di Frascati dell' INFN, *Frascati, Italy*

R. Baldini, A. Calcaterra, R. De Sangro, I. Peruzzi (also Univ. Perugia), M. Piccolo, A. Zallo

INFN, Sezione di Genova and Università di Genova, *Genova, Italy*

A. Buzzo, R. Contri, G. Crosetti, P. Fabbricatore, S. Farinon, R. Monge, M. Olcese, R. Parodi, S. Passaggio, C. Patrignani, M.G. Pia, C. Salvo, A. Santroni

University of Iowa, *Iowa City, Iowa, USA*

U. Mallik, E. McCliment, M.-Z. Wang

Iowa State University, *Ames, Iowa, USA*

H.B. Crawley, A. Firestone, J.W. Lamsa, R. McKay, W.T. Meyer, E.I. Rosenberg

Northern Kentucky University, *Highland Heights, Kentucky, USA*

M. Falbo-Kenkel

University of Lancaster, *Lancaster, UK*

C.K. Bowdery, A.J. Finch, F. Foster

Lawrence Berkeley Laboratory, *Berkeley, California, USA*

G.S. Abrams, D. Brown, T. Collins, C.T. Day, S.F. Dow, F. Goozen, R. Jacobsen, R.C. Jared, J. Kadyk, L.T. Kerth, I. Kipnis, J.F. Kral, R. Lafever, R. Lee, M. Levi, L. Luo, G.R. Lynch, M. Momayezi, M. Nyman, P.J. Oddone, W.L. Pope, M. Pripstein, D.R. Quarrie, J. Rasson, N.A. Roe, M.T. Ronan, W.A. Wenzel, S. Wunduke

Lawrence Livermore National Laboratory, *Livermore, California, USA*

O. Alford, J. Berg, R.M. Bionta, A. Brooks, F.S. Dietrich, O.D. Fackler, M.N. Kreisler, M.A. Libkind, M.J. Mugge, T. O'Connor, L. Pedrotti, X. Shi, W. Stoeffl, K. van Bibber, T.J. Wenaus, D.M. Wright, C.R. Wuest, R.M. Yamamoto

University of Liverpool, *Liverpool, UK*

J.R. Fry, E. Gabathuler, R. Gamet, A. Muir, P. Sanders

University of London, Imperial College of Science, Technology and Medicine, *London, UK*

P. Dornan, A. Duane, L. Moneta, J. Nash, D. Price

University of London, Queen Mary & Westfield College, *London, UK*

D.V. Bugg, P.F. Harrison, I. Scott, B. Zou

University of London, Royal Holloway & Bedford New College, *Egham, Surrey, UK*

Y. Gao, M.G. Green, D.L. Johnson, E. Tetteh-Lartey

University of Louisville, *Louisville, Kentucky, USA*

C.L. Davis

McGill University, *Montréal, Quebec, Canada*

D. Britton, R. Fernholz, D. MacFarlane, P. Patel, C. Smith, B. Spaan, J. Trischuk

University of Manchester, *Manchester, UK*

J. Allison, R. Barlow, G. Lafferty, K. Stephens

University of Maryland, *College Park, Maryland, USA*

C. Dallapiccola, M. Foucher, H. Jawahery, A. Skuja

University of Massachusetts, *Amherst, Massachusetts, USA*

J. Button-Shafer, J.-J. Gomez-Cadenas, S.S. Hertzbach, R.R. Kofler, M.G. Strauss

Massachusetts Institute of Technology, *Cambridge, Massachusetts, USA*

R.F. Cowan, M.J. Fero, R.K. Yamamoto

INFN, Sezione di Milano and Università di Milano, *Milano, Italy*

M. Calvi, C. Cattadori, R. Diaferia, F. Lanni, C. Matteuzzi, F. Palombo, A. Sala, T. Tabarelli

University of Mississippi, *Oxford, Mississippi, USA*

M. Booke, S. Bracker, L. Cremaldi, K. Gounder, R. Kroeger, J. Reidy, D. Summers

Université de Montréal, *Montréal, Quebec, Canada*

G. Beaudoin, M. Beaulieu, B. Lorazo, J.P. Martin, P. Taras, V. Zacek

Mount Holyoke College, *South Hadley, Massachusetts, USA*

H. Nicholson, C.S. Sutton

INFN, Sezione di Napoli and Università di Napoli, *Napoli, Italy*

N. Cavallo, L. Lista, S. Mele, P. Parascandolo, C. Sciacca

University of Notre Dame, *Notre Dame, Indiana, USA*

J.M. Bishop, N.N. Biswas, N.M. Cason, J.M. LoSecco, A.H. Sanjari, W.D. Shephard

Oak Ridge National Laboratory/Y-12, *Oak Ridge, Tennessee, USA*

F.S. Alsmiller, R.G. Alsmiller, Jr., T.A. Gabriel, J.L. Heck

LAL Orsay, *Orsay, France*

D. Breton, R. Cizeron, S. Du, A.-M. Lutz, J.M. Noppe, S. Plaszczynski, M.-H. Schune, E. Torassa, K. Truong, G. Wormser

INFN, Sezione di Padova and Università di Padova, *Padova, Italy*

F. Dal Corso, M. Morandin, M. Posocco, R. Stroili, C. Voci

Ecole Polytechnique Palaiseau, LPNHE, *Palaiseau, France*

L. Behr, G. Bonneaud, P. Matricon, G. Vasileiadis, M. Verderi

LPNHE des Universités Paris 6 et Paris 7, *Paris, France*

M. Benayoun, H. Briand, J. Chauveau, P. David, C. De La Vaissiere, L. Del Buono, J.F. Genat, O. Hamon, P. Leruste, J. Lory, J.-L. Narjoux, B. Zhang

INFN, Sezione di Milano and Università di Pavia, *Pavia, Italy*

P.F. Manfredi, V. Re, V. Speziali, F. Svelto

University of Pennsylvania, *Philadelphia, Pennsylvania, USA*

L. Gladney

INFN, Sezione di Pisa, Università di Pisa[†] and Scuola Normale Superiore[‡], *Pisa, Italy*

G. Batignani[†], S. Bettarini, F. Bosi, U. Bottigli[†], M. Carpinelli, F. Costantini[†],

F. Forti, D. Gambino, M. Giorgi†, A. Lusiani‡, P.S. Marrocchesi, M. Morganti†, G. Rizzo, G. Triggiani†, J. Walsh

Prairie View A&M University, *Prairie View, Texas, USA*

M. Gui, D.J. Judd, K. Paick, D.E. Wagoner

Princeton University, *Princeton, New Jersey, USA*

C. Bula, C. Lu, K.T. McDonald

INFN, Instituto Superiore di Sanità, *Roma, Italy*

C. Bosio

INFN, Sezione di Roma and Università "La Sapienza," *Roma, Italy*

F. Ferroni, E. Lamanna, M.A. Mazzoni, S. Morganti, G. Piredda, R. Santacesaria

Rutgers University, *Rutgers, New Jersey, USA*

P. Jacques, M. Kalelkar, R. Plano, P. Stamer

Rutherford Appleton Laboratory, *Chilton, Didcot, UK*

P.D. Dauncey, J. Dowdell, B. Franek, N.I. Geddes, G.P. Gopal, R. Halsall, J.A. Lidbury, V.J. Perera

CEA, DAPNIA, CE-Saclay,[1] *Gif-sur-Yvette, France*

R. Aleksan, P. Besson, T. Bolognese, P. Bourgeois, A. de Lesquen, A. Gaidot, L. Gosset, G. Hamel de Monchenault, P. Jarry, G. London, M. Turluer, G. Vasseur, C. Yeche, M. Zito

Shanghai Institute of Ceramics (SICCAS), *Shanghai, China*

J.R. Jing, P.J. Li, D.S. Yan, Z.W. Yin

University of South Carolina, *Columbia, South Carolina, USA*

M.V. Purohit, J. Wilson

[1] **Subject to approval of funding agency.**

Stanford Linear Accelerator Center, *Stanford, California, USA*

D. Aston, R. Becker-Szendy, R. Bell, E. Bloom, C. Boeheim, A. Boyarski, R.F. Boyce, D. Briggs, F. Bulos, W. Burgess, R.L.A. Cottrell, D.H. Coward, D.P. Coupal, W. Craddock, H. DeStaebler, J.M. Dorfan, W. Dunwoodie, T. Fieguth, D. Freytag, R. Gearhart, T. Glanzman, G. Godfrey, G. Haller, J. Hewett, T. Himel, J. Hoeflich, W. Innes, C.P. Jessop, W.B. Johnson, H. Kawahara, L. Keller,[2] M.E. King, J. Krebs, P. Kunz, W. Langeveld, E. Lee, D.W.G.S. Leith, V.G. Lüth, H. Lynch, H. Marsiske, T. Mattison, R. Melen, K. Moffeit, L. Moss, D. Muller, M. Perl, G. Oxoby, M. Pertsova, H. Quinn, B.N. Ratcliff, S.F. Schaffner, R.H. Schindler, S. Shapiro, C. Simopolous, A.E. Snyder, E.J. Soderstrom, J. Vav'ra, S. Wagner, D. Walz, R. Wang, J.L. White, W. Wisniewski, N. Yu

Stanford University, *Stanford, California, USA*

P. Burchat, R. Zaliznyak

Academia Sinica, *Taipei, Taiwan*

H.-Y. Chau, M.-L. Chu, S.-C. Lee

University of Texas at Dallas, *Richardson, Texas, USA*

J.M. Izen, X. Lou

INFN, Sezione di Torino and Università di Torino, *Torino, Italy*

F. Bianchi, D. Gamba, G. Giraudo, A. Romero

INFN, Sezione di Trieste and Università di Trieste, *Trieste, Italy*

L. Bosisio, R. Della Marina, G. Della Ricca, B. Gobbo, L. Lanceri, P. Poropat

TRIUMF, *Vancouver, British Columbia, Canada*

R. Henderson, A. Trudel

[2]Retired

Tsinghua University, *Beijing, China*

Y.P. Kuang, R.C. Shang, B.B. Shao, J.J. Wang

Vanderbilt University, *Nashville, Tennessee, USA*

R.S. Panvini, T.W. Reeves, P.D. Sheldon, M.S. Webster

University of Victoria, *Victoria, British Columbia, Canada*

M. McDougald, D. Pitman

University of Wisconsin, *Madison, Wisconsin, USA*

H.R. Band, J.R. Johnson, G.S. Mitchell, R. Prepost, G.H. Zapalac

York University, *Toronto, Ontario, Canada*

W. Frisken

Bibliography

[1] D. Griffiths, *Introduction to Elementary Particles*, (1987), Wiley.

[2] F. Halzen and A. Martin, *Quarks and Leptons*, (1984) Wiley.

[3] L. Montanet *et al*, Particle Data Group, *Particle Physics Book*, (July 1994) American Institute of Physics, Phys. Rev. **D50**, 1173.

[4] P.R. Burchat, *Physics at an Asymmetric-Energy B Meson Factory*, Lake Louise Winter Institute, (1991) Conference Proceedings.

[5] A.D. Sakharov, *The Baryon Asymmetry of the Universe*, (May 1991) Usp. Fiz. Nauk. **161**, 110.

[6] W.S.C. Williams, *Nuclear and Particle Physics*, (1991) Oxford University Press.

[7] F. Wilczek, *The Cosmic Asymmetry Between Matter and Antimatter*, (1980) Sci. Am. **243**, No. 6, 60.

[8] C.S. Wu, E. Ambler, R.W. Hayward, D.D. Hoppes, R.P. Hudson, (1957) Phys. Rev. **D105**, 1413.

[9] L. Wolfenstein, *CP Noninvariance in K^0 Decay*, (June 1985) Comments Nucl. Part. Phys. **14**, 135.

[10] Y. Nir and H.R. Quinn, *Learning about the Cabibbo-Kobayashi-Maskawa matrix from CP asymmetries in B^0 decays*, (1990) Phys. Rev. **D42**, 1473.

[11] The *BaBar* Collaboration, *Letter of Intent for the Study of CP Violation and Heavy Flavor Physics at PEP-II*, (1994) SLAC-443.

[12] The *BaBar* Collaboration, *BaBar Technical Design Report*, (1995) SLAC-R-95-457.

[13] P. Marmier, E. Sheldon, *Physics of Nuclei and Particles*, (1969) Academic Press.

[14] D.C. Carey, K.L Brown and F.C. Iselin, *Decay TURTLE (Trace Unlimited Rays Through Lumped Elements): A computer Program for Simulating Charged Particle Beam Transport Systems, Including Decay Calculations*, (1980) SLAC-246.

[15] C. Hearty, *OBJEGS Users' Manual*, (1991) *BaBar* Note # 73.

[16] *GEANT Detector Description Tool, version 3.21*, CERN Program Library W5103, (1994) CERN.

[17] J. Butcher, *Random sampling from the normal distribution.*, (1961) Computer Journal, **3**, 251.

[18] T. Browder, M. Witherell, *Limits on Backgrounds for the B Factory Detectors*, (1991) *BaBar* Note # 65.

[19] J. Schwinger, *On the Classical Radiation of Accelerated Electrons*, (1949) Phys. Rev. **75**, 1912.

[20] M. Sullivan, *Detector Backgrounds from Synchrotron Radiation*, (1991) SLAC-373.

[21] R. Brun, *HBOOK users guide (Version 4.15)*, Program Library Y250, (1992), CERN.

[22] W.R. Nelson, H. Hirayama, D.W.O. Rogers, *The EGS4 Code System*, (1985) SLAC-265.

[23] *PAW - Physics Analysis Workstation*, Program Library Q121, (1993), CERN.